



HAL
open science

Imbalance of NRG1-ERBB2/3 signalling underlies altered myelination in Charcot–Marie–Tooth disease 4H

Lara El-Bazzal, Adeline Ghata, Clothilde Esteve, Jihane Gadacha, Patrice Quintana, Christel Castro, Nathalie Roeckel-Trévisiol, Frédérique Lembo, Nicolas Lenfant, André Mégarbané, et al.

► To cite this version:

Lara El-Bazzal, Adeline Ghata, Clothilde Esteve, Jihane Gadacha, Patrice Quintana, et al.. Imbalance of NRG1-ERBB2/3 signalling underlies altered myelination in Charcot–Marie–Tooth disease 4H. *Brain - A Journal of Neurology* , 2022, 10.1093/brain/awac402 . hal-03977684

HAL Id: hal-03977684

<https://amu.hal.science/hal-03977684v1>





Submitted on 7 Feb 2023

HAL is a multi-disciplinary open access archive for the deposit and dissemination of scientific research documents, whether they are published or not. The documents may come from teaching and research institutions in France or abroad, or from public or private research centers.

L'archive ouverte pluridisciplinaire **HAL**, est destinée au dépôt et à la diffusion de documents scientifiques de niveau recherche, publiés ou non, émanant des établissements d'enseignement et de recherche français ou étrangers, des laboratoires publics ou privés.



Imbalance of NRG1-ERBB2/3 signalling underlies altered myelination in Charcot–Marie–Tooth disease 4H

Lara El-Bazzal,¹ Adeline Ghata,¹ Clothilde Estève,¹ Jihane Gadacha,¹ Patrice Quintana,¹ Christel Castro,¹ Nathalie Roeckel-Trévisiol,¹ Frédérique Lembo,² Nicolas Lenfant,¹ André Mégarbané,³ Jean-Paul Borg,² Nicolas Lévy,¹  Marc Bartoli,¹  Yannick Poitelon,⁴ Pierre L. Roubertoux,¹  Valérie Delague^{1,†} and  Nathalie Bernard-Marissal^{1,†}

[†]These authors contributed equally to this work.

Charcot–Marie–Tooth (CMT) disease is one of the most common inherited neurological disorders, affecting either axons from the motor and/or sensory neurons or Schwann cells of the peripheral nervous system (PNS) and caused by more than 100 genes. We previously identified mutations in *FGD4* as responsible for CMT4H, an autosomal recessive demyelinating form of CMT disease. *FGD4* encodes FRABIN, a GDP/GTP nucleotide exchange factor, particularly for the small GTPase Cdc42. Remarkably, nerves from patients with CMT4H display excessive redundant myelin figures called outfoldings that arise from focal hypermyelination, suggesting that FRABIN could play a role in the control of PNS myelination. To gain insights into the role of *FGD4*/FRABIN in Schwann cell myelination, we generated a knock-out mouse model (*Fgd4*^{SC-/-}), with conditional ablation of *Fgd4* in Schwann cells. We show that the specific deletion of FRABIN in Schwann cells leads to aberrant myelination *in vitro*, in dorsal root ganglia neuron/Schwann cell co-cultures, as well as *in vivo*, in distal sciatic nerves from *Fgd4*^{SC-/-} mice. We observed that those myelination defects are related to an upregulation of some interactors of the NRG1 type III/ERBB2/3 signalling pathway, which is known to ensure a proper level of myelination in the PNS. Based on a yeast two-hybrid screen, we identified SNX3 as a new partner of FRABIN, which is involved in the regulation of endocytic trafficking. Interestingly, we showed that the loss of FRABIN impairs endocytic trafficking, which may contribute to the defective NRG1 type III/ERBB2/3 signalling and myelination. Using RNA-Seq, *in vitro*, we identified new potential effectors of the deregulated pathways, such as ERBIN, RAB11FIP2 and MAF, thereby providing cues to understand how FRABIN contributes to proper ERBB2 trafficking or even myelin membrane addition through cholesterol synthesis. Finally, we showed that the re-establishment of proper levels of the NRG1 type III/ERBB2/3 pathway using niacin treatment reduces myelin outfoldings in nerves of CMT4H mice.

Overall, our work reveals a new role of FRABIN in the regulation of NRG1 type III/ERBB2/3 NRG1 signalling and myelination and opens future therapeutic strategies based on the modulation of the NRG1 type III/ERBB2/3 pathway to reduce CMT4H pathology and more generally other demyelinating types of CMT disease.

- 1 Aix Marseille Univ, INSERM, MMG, U 1251, Marseille, France
- 2 Aix Marseille Univ, INSERM, CNRS, CRCM, Institut Paoli-Calmettes, Marseille, France
- 3 Department of Human Genetics, Gilbert and Rose-Marie Chagoury School of Medicine, Lebanese American University, Beirut, Lebanon
- 4 Department of Neuroscience and Experimental Therapeutics, Albany Medical College, Albany, NY, USA

Received March 25, 2022. Revised August 30, 2022. Accepted October 02, 2022. Advance access publication October 31, 2022

© The Author(s) 2022. Published by Oxford University Press on behalf of the Guarantors of Brain.

This is an Open Access article distributed under the terms of the Creative Commons Attribution-NonCommercial License (<https://creativecommons.org/licenses/by-nc/4.0/>), which permits non-commercial re-use, distribution, and reproduction in any medium, provided the original work is properly cited. For commercial re-use, please contact journals.permissions@oup.com

Correspondence to: Valérie Delague
Marseille Medical Genetics
U 1251, Aix Marseille Université
Faculté de Médecine de la Timone
27 bd Jean Moulin, 13385 Marseille cedex 05, France
E-mail: valerie.delague@univ-amu.fr

Keywords: Charcot–Marie–Tooth; myelin outfoldings; endocytic trafficking; NRG1/ERBB2/3; niacin treatment

Introduction

Charcot–Marie–Tooth (CMT) disease, also known as hereditary motor and sensory neuropathy (HMSN), is one of the most common inherited group of neurological diseases, with an overall prevalence of about 1/2500.¹ Clinically, CMT diseases are characterized by progressive muscular weakness starting at the distal extremities, pes cavus deformity, loss of deep tendon reflexes, associated with mild to moderate distal sensory loss.² Two main subgroups can be defined based on electrophysiological and histopathological characteristics: the demyelinating form (CMT1) resulting from primary damage of myelinating Schwann cells (SCs) and the axonal form (CMT2), affecting the axons from motor (MNs) and/or sensory neurons (SNs). Patients affected with CMT1 have reduced nerve-conduction velocities (NCVs; ≤ 38 m/s), whereas patients affected with CMT2 show slightly reduced to normal NCVs but reduced amplitudes (≥ 38 m/s).³ In addition, CMT disease is characterized by extensive clinical and genetic heterogeneity, with around 100 genes identified to date and mutations segregating following all modes of inheritance.⁴

In 2007, we and others identified *FGD4/FRABIN* as the causative gene of CMT4H,⁵ a rare autosomal recessive demyelinating form of CMT.^{6,7} The disease is characterized by typical findings of CMT, such as distal amyotrophy and foot deformities, with early-onset and slow progression. Motor and sensory NCVs are strongly reduced in all patients, but there is a strong inter- and intra-familial variability in the severity of the disease. The diagnosis is established by the presence of biallelic pathogenic variants in the *FGD4* gene, encoding the protein FRABIN. More than 30 mutations are described to date in *FGD4*, most of them resulting in a loss of the protein or a non-functional truncated protein.^{6,8,9} Remarkably, nerves from patients affected with CMT4H display characteristic myelin abnormalities defined as myelin outfoldings, which arise from aberrant focal hypermyelination. In the peripheral nervous system (PNS), the myelination process is mainly regulated by the NRG1 type III/ERBB2/3 pathway: notably, the amount of axonal NRG1 type III and its downstream signalling, via the activation of the ERBB2/3 receptors, determines the thickness of the myelin sheath.^{10,11} In consequence, this pathway has to be tightly regulated to avoid improper myelination. Previous work has reported that myelin outfoldings might arise from an enhanced NRG1 type III/ERBB2/3 signalling, as well as the overactivation of the downstream effectors AKT/mTOR.^{12–14} A growing body of work suggests that the dysregulation of ERBB receptor trafficking may be the cause of an impairment of NRG1 type III/ERBB2/3 signalling in SCs and a common pathogenic mechanism for several CMT4 subtypes, such as CMT4B1 (OMIM #601382), CMT4B2 (OMIM #604563), CMT4C (OMIM #601596)^{15,16} and CMT4D (OMIM #601455).¹⁷ However, in CMT4H, the implication of FRABIN in the regulation of PNS myelination and the above-mentioned signalling pathways remains poorly studied.

FRABIN is a ubiquitously expressed protein containing five functional domains: a Dbl domain, responsible for the guanine exchange factor (GEF) activity toward CDC42 and RAC1, an N-terminal F-actin binding domain and three domains [two pleckstrin homology (PH) and one FYVE domain] implicated in binding to phosphoinositides (PIs).^{18,19} PIs are known regulators of endocytic trafficking²⁰ and previous work by Horn et al.²¹ has shown an impairment of endocytosis in the absence of FRABIN, without providing a link to the aberrant hypermyelination in CMT4H.

We hereby provide evidence that FRABIN is required for proper myelination of the PNS by regulating NRG1 type III/ERBB2/3 signalling in both *in vitro* and *in vivo* models of CMT4H. In particular, we show that the specific deletion of FRABIN in SCs leads to aberrant myelination *in vitro*, in dorsal root ganglia (DRG) neurons/SCs co-cultures and *in vivo*, in distal sciatic nerves of conditional knock-out mice. We demonstrate that the myelination defects in CMT4H are related to impaired NRG-1 type III/ERBB2/3 signalling and defective endocytic trafficking. Finally, we show that the re-establishment of proper levels of the different actors of the NRG1 type III/ERBB2/3 pathway, using niacin treatment, reduces the proportion of myelin outfoldings in nerves of our CMT4H mouse model.

Material and methods

Animals

To generate a conditional *Fgd4* null allele, we first generated a mouse with a floxed allele by flanking *Fgd4* exon 4 with *lox-P* sites. Its excision, by crossing with a transgenic mouse expressing the Cre-recombinase, introduces a frameshift and is predicted to generate a premature stop codon in exon 5. Mice heterozygous for the *Fgd4* floxed allele (*Fgd4^{fl/+}*) have been developed on a pure C57BL/6N background in collaboration with 'La Clinique de la Souris' (ICS; Strasbourg; <http://www.ics-mci.fr>) by performing homologous recombination in embryonic stem cells (ES) derived from C57BL/6N mouse. The *Fgd4^{fl/+}* line was maintained on a pure C57BL/6N background (Taconic Biosciences A/S, Denmark). Genotyping of *Fgd4^{fl/+}* mice was performed by PCR on DNA isolated from tail biopsies using direct PCR lysis reagent (#VI-102-T, Viagen Biotech Inc.), following the manufacturer's instructions, using the primers flox-LF (5'-CGAACCCCTTAGCGATCTGTT-3') and flox-LR (5'-TTTTCCTAGCTGGCGTGT-3').

To obtain an allele with specific deletion of *Fgd4* in SCs, we crossed *Fgd4^{fl/+}* mice with transgenic mice expressing the Cre-recombinase under a promoter-specific for SCs [B6N.FVB-Tg(Mpz-cre)26Mes/J], 'so-called P0-Cre mice', available at the Jackson Laboratories (#017927).²² We obtained *Fgd4^{fl/+}*; P0-Cre, so-called *Fgd4^{SC-/-}* that we backcrossed for at least 10 generations on C57BL/6N (Taconic) background. The P0-Cre transgene was detected by PCR using the following primers: P0Cre-F (5'-CCACCACCTCTCCATTGGAC-3') and P0Cre-R (5'-GCTGGCCCAA

ATGTTGCTGG-3'). For ubiquitous deletion of *Fgd4*, *Fgd4^{fl/+}*; CMV-Cre, mice, so-called *Fgd4^{-/-}*, were generated by crossing the floxed *Fgd4^{fl/+}* line with transgenic mice expressing the Cre-recombinase under the CMV promoter [B6.C-Tg (CMV-cre) 1Cgn/J], available at the Jackson Laboratories (#006054). The CMV-Cre transgene was detected by PCR using the following primers: CMVCre-F (5'-AGGTTGTTCACTCATGA-3') and CMVCre-R (5'-TCGACCAGTTTAGTTACCC-3'). The excision of the exon 4 in the *Fgd4^{-/-}* mice was detected using the primers flox-LF (5'-CGAACCTTAGCGATCTGTT-3') and flox-ER (5'-CAAGCCTCAGCTTCACTTCC-3'). Animals were housed in an animal facility with a 12 h light/12 h dark environment and *ad libitum* access to water and a normal diet. All experiments were done in accordance with a national appointed ethical committee for animal experimentation (Ministère de l'Éducation Nationale, de l'Enseignement Supérieur et de la Recherche; Authorization No. 2019062110352453 v4).

Niacin treatment

One-month-old *Fgd4^{SC-/-}* mice were injected daily with saline solution or niacin (60 mg/kg) for 8 weeks ($n = 4$ saline-treated animals and 5 niacin-treated animals). Nicotinic acid (#PHR1276, Niacin, Sigma-Aldrich) was diluted in sterile saline solution and was daily injected intraperitoneally at a dose of 60 mg/kg.

Primary cell culture

Schwann cells culture

Primary rat SCs were prepared from the sciatic nerves of postnatal Day 3 pups. SCs were maintained in Dulbecco's Modified Eagle's Medium (#41965039 ThermoFisher Scientific), 2 mM L-glutamine (#25030024, ThermoFisher Scientific), 10% foetal bovine serum (FBS; #10270098, ThermoFisher Scientific), 2 μ M forskolin (#344270, Merck) and 2 ng/ml recombinant human NRG1- β 1 (#396-HB, R&D Systems) as described in Poitelon *et al.*²³ SCs were not used beyond the fourth passage.

DRG neurons/SCs co-cultures

Mouse DRG neurons were isolated after dissecting the spinal cord of embryonic Day 13.5 (E13.5) embryos and seeded on 12 mm glass coverslips, as described.²³ In detail, after isolation, DRGs were dissociated and then incubated in 0.25% trypsin solution (#25200056, ThermoFisher Scientific) for 45 min at 37°C. DRGs were mechanically dissociated and ~40 000 cells were seeded on matrigel- (#356234, Corning) coated coverslips in C-medium, composed of minimum essential medium (MEM) (#11090081, ThermoFisher Scientific), 2 mM L-glutamine (#25030024, ThermoFisher Scientific), 10% FBS (#10270098, ThermoFisher Scientific), 4 mg/ml D-glucose (#G5146, Sigma-Aldrich), 50 ng/ml nerve growth factor (NGF) (#N6009, Sigma-Aldrich). After 24 h, the C-medium was replaced by NB medium, composed as follows: neurobasal medium (#21103049, ThermoFisher Scientific), 4 g/l D-glucose (#G5146, Sigma-Aldrich), 2 mM L-glutamine (#25030024, ThermoFisher Scientific), 50 ng/ml NGF (#N6009, Sigma-Aldrich) and B27 supplement 1 \times (50 \times , #17504044, ThermoFisher Scientific) and changed every 2 days. After 5 days of NB medium, myelination was induced by adding 50 μ g/ml ascorbic acid (#A0278, Sigma-Aldrich) to the C-medium for 12 days.

Drugs

Co-cultures were treated using nicotinic acid (niacin, #PHR1276, Sigma-Aldrich) diluted in MEM (#11090081, ThermoFisher Scientific) at a final concentration of 5 mM. Endosidin-2 (ES2; #SML168, 5 mg, Sigma-Aldrich) was diluted in MEM at a final concentration of 1 μ M. Niacin or ES2 were added concomitantly to ascorbic acid at Day 6 of the co-culture.

Analysis of myelination

Around 10 fields per coverslip were randomly acquired with a Zeiss ApoTome.2 microscope (Zeiss) using a $\times 20$ objective. Myelin abnormalities were defined as an excessive redundant or abnormal thickening of myelin visualized along with myelin basic protein (MBP) positive segments and quantified in ~150–160 myelinated segments for each co-culture and at least three co-cultures. Results were expressed as a percentage of MBP-positive segments showing myelin abnormalities on the total of MBP-positive fibres.

RNA sequencing

RNA-sequencing and bioinformatics analysis was performed by the Genomics and Bioinformatics facility (GBiM) from the U1251/Marseille Medical Genetics laboratory. mRNA sequencing (mRNA-Seq) was performed, in duplicate, on total RNA samples extracted from DRG/SC co-cultures derived from either conditional knockout (*Fgd4^{SC-/-}*) or wild-type (WT) littermates' embryos (four samples in total). Total RNA was extracted from each condition (two coverslips of control *Fgd4^{fl/fl}* and *Fgd4^{SC-/-}* DRG/SC co-cultures, in two replicates), using Purelink silica membrane, anion exchange resin, spin-column kits, following the manufacturer's recommendations (Purelink RNA Minikit, #12183018A, ThermoFisher Scientific). Before sequencing, the quality of total RNA samples was assessed using the Agilent Bioanalyzer (Agilent Technologies): only RNAs with RNA Integrity Numbers (RIN) above 8 were deemed suitable for sequencing and used for library preparation. For each sample, a library of stranded mRNA was prepared from 500 ng of total RNA after capture of RNA species with poly-A tail poly(A), using the Kapa mRNA HyperPrep kit (Roche), following the manufacturer's instructions. The quality and profile of individual libraries have been quantified and visualized using Qubit™ and the Agilent Bioanalyzer dsDNA High Sensibility Kit (Agilent Technologies), respectively. Indexed libraries were pooled and sequenced (2 \times 75 bp paired-end sequencing) on an Illumina NextSeq 500 platform (Illumina).

Data processing and differential gene expression analysis

The quality of sequencing reads was assessed using fastQC v0.11.5 (<https://www.bioinformatics.babraham.ac.uk/projects/fastqc/>). Raw sequencing reads were mapped to the mouse reference genome (*Mus musculus*) genome assembly GRCm38 (mm10) using STAR v2.5.3a²⁴ and bam files were indexed and sorted using Sambamba v0.6.6.²⁵ After mapping, the number of reads per feature (GENCODE v34 annotations) was determined using Stringtie v1.3.1c.²⁶ Differential gene expression analysis was performed using a Wald test thanks to the DESeq2 package.²⁷ P-values were adjusted for multiple testing using the method described by Benjamini and Hochberg (BH).²⁸ Only transcripts with an adjusted P-value (false discovery rate, FDR) below 0.05 were considered as significantly differentially expressed. Relative expressions of the

most variable features between samples have been plotted as heat maps using the Pheatmap R package. Differentially expressed genes (DEGs) were visualized in the form of volcano plots, representing the Log_2FC (log2 of the expression fold change) and the adjusted P-value, prepared using the EnhancedVolcano R package. Enrichment (gene set enrichment Analysis, GSEA) and overrepresentation (singular enrichment analysis, SEA) of Gene Ontology (GO) term annotation in the DEGs were performed using a Mann–Whitney test and hypergeometric test, respectively, using enrichGO from the R-package clusterProfiler (v3.10.15). For functional GO annotation, we selected the DEGs with a statistical significance of *P*adj value < 0.05 (SEA). Pathway analysis was conducted, using Reactome, which uses a hypergeometric test with an adjustment of the P-value (BH) to detect pathway, enriched in the data set of DEGs from the top10 GO biological process (BP) terms.

Statistical analyses

The applied statistical tests, as well as the number of replicates, are indicated in the figure legends. For all experiments based on primary co-cultures, results were obtained from at least three independent cell cultures.

Animals were matched by gender, genotype and age. Mice were randomly assigned to experimental groups and gait experiments, as well as processing and analysis of the tissues, were performed in blind. The significance of the results for electron microscopy, primary cultures and *in vivo* niacin treatment was evaluated with one- or two-way ANOVA or two-tailed Student's *t*-test according to experimental design. Statistical analyses were performed using GraphPad Prism. All data are presented as mean \pm SEM.

For gait analysis, each mouse was characterized by the median score of the left and right paw for motor function studies. The scores were analysed according to the ANCOVA statistics with weight at the corresponding age as a covariate, using²⁹ and SPSS Statistics 19.³⁰ We calculated the effect size and its confidence interval. Results were expressed as means and SEM.

Data availability

The authors confirm that the data supporting the findings of this study are available within the article and/or its [Supplementary material](#). These data are available from the corresponding author upon reasonable request.

Results

Specific loss of FRABIN in Schwann cells induces myelin abnormalities *in vitro* and *in vivo*

To determine the pathomechanisms underlying CMT4H disease, we generated mice with an *Fgd4* floxed allele, in order to study the effect of *Fgd4* ablation in the different cell types constitutive of the PNS (i.e. motor and DRG neurons and Schwann cells), by crossing them with transgenic mice expressing Cre-recombinase under the requested cell-specific promoter (Fig. 1A). To this aim, the exon 4 of *Fgd4* was flanked with LoxP sites by homologous recombination. Because previous work from Horn *et al.*²¹ showed that the clinical phenotype and the molecular basis of CMT4H relied on the loss of function of FGD4/FRABIN in SCs, without detectable primary contributions from neurons, we generated a conditional null allele mouse model, referred to as *Fgd4*^{SC-/-}, by abolishing FRABIN's expression specifically in SCs. Conditional ablation of *Fgd4* in SCs was obtained by mating mice homozygous for

the floxed allele (*Fgd4*^{fl/fl}) with transgenic P0-Cre mice to drive expression of the Cre-recombinase in SCs at E13.5.²² We demonstrated the effective deletion of the floxed exon 4 in this conditional knockout *Fgd4*^{SC-/-} mouse model, by RT-PCR, using total RNA extracted from sciatic nerves of *Fgd4*^{SC-/-} and control mice (Fig. 1B and C). As expected, we show that the deletion of exon 4 leads to a shorter fragment amplified between exons 3 and 7, in the mutant nerves (374 bp in *Fgd4*^{SC-/-} versus 882 bp in the WT). Due to the lack of antibodies recognizing specifically mouse FRABIN, we were, unfortunately, unable to assess the deletion by western blot.

We previously observed that the loss of FRABIN leads to aberrant myelin structures called outfoldings in nerves of patients affected with CMT4H.^{5,6,9} Here, we wanted to assess whether such abnormalities could be reproduced in our *Fgd4*^{SC-/-} mouse model both *in vitro* and *in vivo*. *In vitro*, we established DRG/SC co-cultures from E13.5 *Fgd4*^{SC-/-} embryos, in which myelination was induced for 15 days using ascorbic acid. Myelinated segments were visualized by MBP immunostaining (Fig. 1D and E). Indeed, we noticed irregularly shaped MBP-positive fibres reflecting focal hypermyelination (Fig. 1E), similar to those previously described in a co-culture model derived from the mouse model for CMT4B1.^{13,31} In *Fgd4*^{SC-/-} DRG/SC co-cultures, the proportion of these abnormal MBP+ fibres represented 71.4 \pm 4.3% of total MBP+ fibres, as compared to control co-cultures, where they represent 21.6 \pm 8.3% (Fig. 1D). To determine whether the presence of those myelin defects was related to a loss of *Fgd4*/FRABIN, we overexpressed *Fgd4*/FRABIN in our mutant *Fgd4*^{SC-/-} co-culture model using lentivirus (Lv). Overexpressing *Fgd4*/FRABIN led to a significant decrease in the proportion of abnormal MBP+ segments in mutant *Fgd4*^{SC-/-} co-cultures (39.8 \pm 5.6%) to a level comparable to control conditions (23.1 \pm 2.9%; Fig. 1F). This finding confirms that the loss of *Fgd4*/FRABIN in SCs is a major contributor to the altered myelin phenotype.

Altered myelination was in parallel evaluated, over-time, *in vivo*, in the sciatic nerves of both *Fgd4*^{SC-/-} and control mice. We observed out- and infoldings, as described in the nerves of CMT4H patients^{5,7-9} (Fig. 1H) and confirming the observations by Horn *et al.*²¹ in their CMT4H mouse model, where a Dhh promoter was used to drive Cre recombinase expression, leading to *Fgd4* ablation specifically in Schwann cells. The proportion of abnormal myelinated fibres was higher in *Fgd4*^{SC-/-} nerves as compared to controls, as soon as 3 months old, and increased significantly over time (3 months old: control 0 \pm 0.1% and *Fgd4*^{SC-/-} 4.9 \pm 1.9%; 6 months old: control 0.46 \pm 0.32% and *Fgd4*^{SC-/-} 9.1 \pm 5.1%; 18 months old: control 0.44 \pm 0.26% and *Fgd4*^{SC-/-} 11.7 \pm 2.1%; Fig. 1G and H). The presence of altered myelin was, however, not correlated to a defect of myelin thickness, as attested by similar g-ratios in mutant versus control sciatic nerves at all studied time points (Fig. 1I and Supplementary Fig. 1A). Finally, in addition to myelination defects, 12-month-old *Fgd4*^{SC-/-} mice display significant denervation of the neuromuscular junctions (NMJs) of the gastrocnemius muscle (% of fully innervated NMJs: WT 75.3 \pm 3.1% versus *Fgd4*^{SC-/-} 50.3 \pm 7%; % of intermediate NMJs: WT 14.5 \pm 1.9% versus *Fgd4*^{SC-/-} 27.06 \pm 6.6% and % of denervated NMJs: WT 10.1 \pm 1.4% versus *Fgd4*^{SC-/-} 22.6 \pm 1.6%), suggesting late distal axonal degeneration (Supplementary Fig. 1B and C).

To assess the locomotor performance of our CMT4H model, we monitored footprint analyses using the gait test at 6, 12 and 18 months. For measures of intensity parameters on which the body mass could have an impact, an ANCOVA was performed, using the genotype as a fixed factor (*Fgd4*^{SC-/-} versus respective control) and body mass as covariate, at the three ages. In 18-month-old

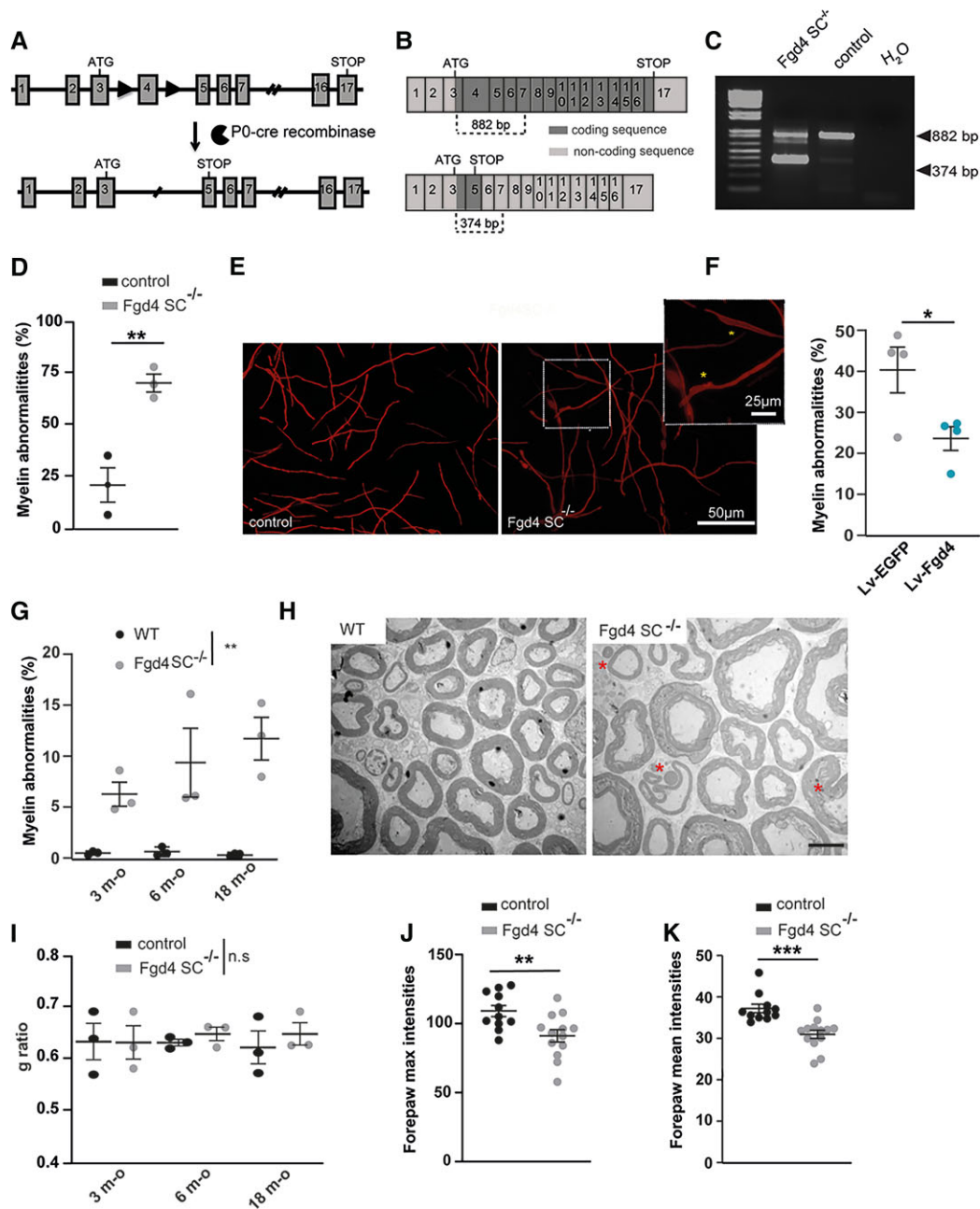


Figure 1 Generation and phenotypic characterization of a new mouse model of CMT4H. (A–C) Generation of a conditional knockout mouse model for CMT4H. (A) The floxed allele (*Fgd4*^{fl/+}) was generated by flanking exon 4 with loxP sites (black arrowheads) in the *Fgd4* gene leading to a frameshift by generation of a premature stop codon in exon 5. The conditional deletion of *Fgd4* in SCs is induced by crossing *Fgd4*^{fl/β} mice with mice expressing the cre recombinase under the *Mpz/P0* promoter. For simplification the conditional knockout *Fgd4*^{fl/β}; *P0cre* mice are referred to as *Fgd4*^{SC-/-}. (B) *Fgd4* transcript before (top) or after (bottom) excision of exon 4 following cre-recombinase expression. (C) Excision of the exon 4 from *Fgd4* transcript was verified by RT-PCR using RNA extracted from the sciatic nerves of *Fgd4*^{SC-/-} and control mice. Due to exon 4 excision, the size of the amplified amplicon was 882 bp and 374 bp in WT and *Fgd4*^{SC-/-} sciatic nerves, respectively. (D and E) Loss of *Fgd4*/FRABIN alters myelination *in vitro*. (D) Number of myelin anomalies quantified in WT and *Fgd4*^{SC-/-} co-cultures. The presence of focal hypermyelination defects was evaluated in 150–160 myelinated segments per coverslip and three independent cultures. Myelinated segments were visualized by immunolabelling of MBP. Data are expressed as mean ± SEM. Statistical analysis: two-way ANOVA with Sidak *post hoc* test. (E) Illustration of myelinated segments in control and *Fgd4*^{SC-/-} co-cultures. Examples of myelin abnormalities that can be observed in the enlarged image and identified by asterisks. (F) Overexpression of *Fgd4*/FRABIN in *Fgd4*^{SC-/-} co-cultures reduces the proportion of abnormally myelinated fibres. *Fgd4*^{SC-/-} co-cultures were infected with Lv-EGFP or Lv-*Fgd4*, 1 day after seeding. Data are expressed as mean percentage ± SEM (*n* = 4 independent cultures). Statistical analysis: unpaired Student's *t*-test. (G and H) Loss of *Fgd4*/FRABIN alters PNS myelination *in vivo*. (G) Proportion of abnormal myelinated fibres in the distal part of the sciatic nerve of 3-, 6- and 18-month-old WT and *Fgd4*^{SC-/-} mice (*n* = 3 animals per genotype). Data are expressed as mean percentage ± SEM. Statistical analysis: two-way repeated-measures ANOVA (group × time) with Sidak *post hoc* test. (H) Electron microscopy pictures illustrating myelination of sciatic nerves of WT (left) and *Fgd4*^{SC-/-} (right) mouse. Asterisks indicate outfoldings. Scale bar = 5 μm. (I) g-Ratio analysis revealed no statistical difference in myelin thickness in the sciatic nerve of at 3-, 6- and 18-month-old WT and *Fgd4*^{SC-/-} mice. A total of 500–1000 axons between 0.5 and 6 μm for animals (*n* = 3 per genotype) were analysed. Data are presented as mean ± SEM (*n* = 3 animals). (J and K) Maximum and mean forepaw intensities are significantly decreased in *Fgd4*^{SC-/-} mice compared to WT mice. Data are expressed as mean ± SEM (*n* = 11 WT and *n* = 13 *Fgd4*^{SC-/-} mice). **P* < 0.05, ***P* < 0.01, ****P* < 0.001.

mice, we detected impaired motor functions, as evidenced by a difference in parameters reflecting the pressure exerted by each paw (i.e. intensity parameters). Indeed, the maximal forepaw intensity was lower in *Fgd4^{SC-/-}* mice (92.4 ± 3.9) compared to controls (110.6 ± 4.8) [$F(1,24) = 8.37$, $P < 0.008$] as well as the mean forepaw intensity: 31.08 ± 0.7 for *Fgd4^{SC-/-}* versus 37.7 ± 1.6 for WT [$F(1,24) = 17.28$, $P < 0.001$]. These differences exceed the limits between pathology and typicality as shown by the large effect's sizes ($\eta^2 = 0.28$, CI from 0.11 to 0.57 and $\eta^2 = 0.43$, CI from 0.19 to 0.53, respectively; Fig. 1J and K).

Specific loss of FRABIN in SCs leads to a deregulation of the neuregulin1 type III-ERBB2/3 myelination pathway

Previous studies reported that myelin outfoldings might arise from an enhanced NRG1 type III/ERBB2/3/AKT/mTOR pathway activation.^{12,13} Therefore, we assessed, by western blot, the level of expression of key components of this pathway, both *in vitro* and *in vivo* (Fig. 2 and Supplementary Fig. 5). *In vitro*, we noticed a significant increase in the levels of the phosphorylated Erbb2 receptor (P-ERBB2), phosphorylated AKT (P-Akt) and mTOR, in *Fgd4^{SC-/-}* co-cultures as compared to control (Fig. 2A and B and Supplementary Fig. 5A–G). The level of full-length and cleaved forms of NRG-1 type III was not significantly different *in vitro* (Supplementary Fig. 1D and E and Supplementary Fig. 6I and J). Abnormal regulation of the NRG1 type III-ERBB2/3 pathway was confirmed *in vivo*, in the sciatic nerves of full knockout mice (*Fgd4^{-/-}*). We used full knockout animals (*Fgd4^{-/-}*), rather than conditional knockout animals (*Fgd4^{SC-/-}*) because, in the latter, the normal expression of Frabin in the axons (which are not knockout) may compensate for any change in the level of expression of the NRG1 type III/Erbb2/3 pathway due to the knockout in Schwann cells. In *Fgd4^{-/-}* sciatic nerves, we observed, by western blot, a significant upregulation of ERBB2 and mTOR, as compared to control nerves, while levels of AKT and its phosphorylated form were not different (Fig. 2C and D and Supplementary Fig. 5H–M). We also noticed a significant decrease of the full-length NRG1 type III (i.e. the pro-protein) and a concomitant increase of the levels of the C-terminal NRG1 fragment,³² which indicates an increase in the cleavage of the NRG1 type III pro-protein (Supplementary Fig. 1F and G and Supplementary Fig. 6K and L). Overall, those observations demonstrate an enhanced activation of the NRG1 type III/ERBB2/3/AKT/mTOR pathway.

Loss of FRABIN does not affect the myelination-related gene expression programme

To examine global gene expression involved in the myelination abnormalities linked to the absence of FRABIN in SCs, we performed bulk mRNA-sequencing on duplicates from *Fgd4^{SC-/-}* and WT co-cultures. The heat map of unsupervised hierarchical clustering of the four samples (two *Fgd4^{SC-/-}* and two WT) showed that the *Fgd4^{SC-/-}* samples clustered separately from the controls (Fig. 3A). GSEA on the entire set of expression data highlighted a total of 2451 genes DEGs between *Fgd4^{SC-/-}* and WT co-cultures. Among them, 1679 were overexpressed and 772 underexpressed (Fig. 3B).

Functional GO annotation of the DEGs, with statistical significance of *P*adj value < 0.05 , showed enrichment in several BPs. Interestingly, in the top enriched BP GO terms, we found 'positive regulation of protein kinase activity' (GO:0045860), 'regulation of GTPase activity' (GO:0043087), 'second-messenger-mediated

signalling' (GO:0019932) or 'cell-substrate adhesion' (Fig. 3C), which are related to the known functions of FRABIN (regulation of GTPase, binding to PIs) and important processes in myelination. Enrichment analysis of the reactome pathways using the list of the 536 DEGs from the top 10 enriched GO terms confirmed major deregulations in signal transduction in *Fgd4^{SC-/-}* co-cultures. As expected, considering the known function of FRABIN as a GEF for small RhoGTPases, we observed enrichment of genes encoding proteins involved in the RAC1 GTPase cycle (#R-HSA-9013149), Rho GTPase cycle (#R-HSA-9012999) and intracellular signalling by second messengers (#R-HSA-9006925; Fig. 3D). In addition, this analysis of pathway enrichment highlights new signalling transduction pathways, which might be important for proper myelination, such as integrin cell surface interactions (Fig. 3D).

In-depth analysis of DEGs from the top enriched GO terms revealed several deregulated genes, such as members of the integrin family (in particular *Itgb8*), members of the G protein-coupled receptor (Gpcr) family, such as *Gpr65*, or other signalling proteins (*Nfat5*, *Tnf*, *Cybb*, *stab1*; Supplementary Table 1). These genes are highlighted in Fig. 3B. We did not reveal any changes of expression in NRG1 type III/ERBB2/3 pathway and associated canonical downstream pathways, nor in myelin structural genes (Supplementary Table 1). However, very interestingly, we observed a significant change of expression of *Maf* ($FC = 1.57$, $P_{adj} = 8.2 \times 10^{-5}$) in *Fgd4^{SC-/-}* co-cultures, a transcription factor acting downstream of the neuregulin signalling and regulating cholesterol biosynthesis in Schwann cells³³ (Supplementary Table 1). Also, there was a significant upregulation of *Erbin* ($FC = 1.65$, $P_{adj} = 0.000341$), a protein interacting with ERBB2, which regulates ERBB2's function and localization at the membrane.³⁴ Finally, we noticed an upregulation of *Rab11fip2* ($FC = 1.69$, $P_{adj} = 0.000378$), a regulator of membrane trafficking.^{35,36}

Interestingly, we were able to confirm that the protein levels of ERBIN are significantly increased in the sciatic nerves of 1-year-old *Fgd4^{-/-}* animals in comparison to control animals (Supplementary Fig. 2A and B).

Specific loss of FRABIN in Schwann cells impairs endosomal trafficking

Emerging data propose that dysregulation of ERBB receptor trafficking may be the cause of the impairment of NRG type III/ERBB2/3 signalling in SCs and represent a common pathogenic mechanism in several CMT4 subtypes.¹⁵ FRABIN is a GEF responsible for GDP/GTP exchange on the small RhoGTPases CDC42 and RAC1, and also contains two PH and one FYVE domains, which are implicated in interactions with PIs. PIs are lipid regulators of endocytic trafficking.²⁰ Previous work by Horn et al.²¹ has shown an impairment of endocytosis in the absence of FRABIN, but its impact on myelination defects has not been studied. To determine whether the myelination defects observed in the *Fgd4^{SC-/-}* mice are connected to defective endocytic trafficking, we looked at the expression of the early endosomal marker RAB5 and the recycling endosomal marker RAB11, *in vitro*. In *Fgd4^{SC-/-}* co-cultures, RAB5 expression levels are increased compared to controls but without reaching statistical significance. In contrast, RAB11 is significantly upregulated in *Fgd4^{SC-/-}* co-cultures compared to control (Fig. 4A and B and Supplementary Fig. 5N–Q). To follow more precisely the endocytic trafficking following FRABIN's loss, we monitored the trafficking of pHrodo-transferrin (pHrodo-TF), over time, in primary SCs knocked-down (KD) for *Fgd4*/FRABIN, as well as in control cells. We induced *Fgd4*/FRABIN KD using a shRNA targeting *Fgd4*

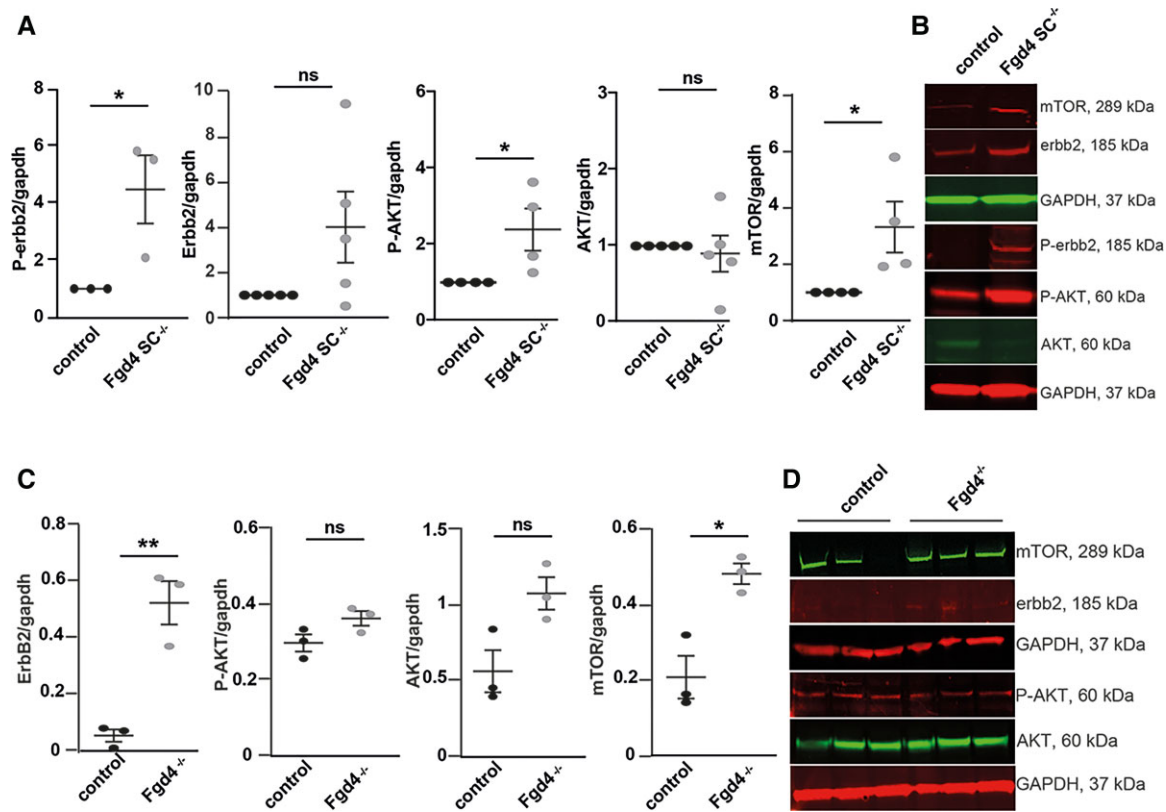


Figure 2 Neuregulin-1 type III/ERBB2/3/AKT/mTOR pathway is upregulated in CMT4H models. (A and B) Phosphorylated ERBB2 (P-ERBB2) and AKT (P-AKT) as well as mTOR expression are significantly increased in *Fgd4*^{SC^{-/-}} co-cultures compared to control. (A) Levels of expression of P-ERBB2, ERBB2, P-AKT, AKT and mTOR were assessed by western blot analysis. Data are expressed as mean \pm SEM ($n = 3-4$ co-cultures) and normalized to the control values. Statistical analysis: unpaired Student's t-test. (B) Western blot pictures illustrating the expression of the markers described in A. (C and D) Levels of expression of P-ERBB2, ERBB2, P-AKT, AKT and mTOR were assessed by western blot analysis in the sciatic nerves of *Fgd4*^{-/-} mice compared to WT mice. (C) Data are expressed as mean \pm SEM ($n = 3$ animals per genotype). Statistical analysis: unpaired Student's t-test. (D) Western blot pictures illustrating the expression of the markers described in C. * $P < 0.05$, ** $P < 0.01$, *** $P < 0.001$.

(SHFgd4), previously described by Horn *et al.*,²¹ delivered in rat primary SCs, using a Lv (Supplementary Fig. 3C). SCs were then pulse-labelled, 48 h post-infection, with fluorescent pHrodo-TF for 30 min at 4°C to prevent uptake and then chased by incubating at 37°C to allow uptake (15 min) and recycling (30 and 45 min). pHrodo-TF has the property to become fluorescent once internalized in the endosomes. By quantifying the levels of fluorescence of pHrodo-TF, we noticed similar levels of internalized TF in SCs expressing a control shRNA (SHcontrol) or SHFgd4, after 15 min of incubation, suggesting a similar capacity of TF-endocytosis between the control and *Fgd4* KD conditions (Fig. 4C and D). In both control and *Fgd4* KD conditions, the level of fluorescence of pHrodo-TF decreases over time due to TF recycling back to the membrane. Interestingly, in comparison to the control conditions, the levels of fluorescence of pHrodo-TF are significantly lower after 45 min of incubation in *Fgd4* KD conditions (SHcontrol: 7.7 ± 1.3 a.u. and SHFgd4: 2.07 ± 0.4 a.u.; Fig. 4C and D). This decrease in TF-retention in the endosomes suggested an increase of pHrodo-TF recycling back to the membrane in conditions of loss of *Fgd4*/FRABIN.

To assess whether the observed endocytic trafficking defect could participate in the improper myelination observed in the *Fgd4*^{SC^{-/-}} co-cultures, we treated the co-cultures with ES2 (1 μ M), a compound known to reduce exocytosis and endosomal recycling.³⁷ Interestingly, treating *Fgd4*^{SC^{-/-}} co-cultures with ES2 decreases

significantly the number of myelin abnormalities observed in conditions of loss of FRABIN (non-treated *Fgd4*^{SC^{-/-}}: $47 \pm 6.8\%$, ES2-treated *Fgd4*^{SC^{-/-}}: $17.5 \pm 5.7\%$; Fig. 4E). Altogether, these data support a defect in endosomal trafficking following *Fgd4*/FRABIN loss, which may compromise proper myelination signalling and contribute to the abnormal myelination observed *in vitro* (Supplementary Fig. 4).

Sorting nexin 3, a new partner of FRABIN, contributes to CMT4H pathogenesis

As the function of FRABIN in vesicle trafficking remains poorly studied, we searched for FRABIN interactors that could be involved in this process. To achieve this, we performed a yeast two-hybrid (Y2H) screening analysis in a human foetal brain library, using *Fgd4* cDNA as bait. Among the partners identified, we focused on Sorting nexin 3 (SNX3). SNX3 belongs to the Sorting nexin protein family, implicated in membrane trafficking. SNX3 is associated with the early endosomes through its PX domain and interacts, as FRABIN, with the polyphosphoinositide PI3P.³⁸ In addition, SNX3 is known to facilitate the recycling of the transferrin receptor.³⁹ We first assessed the localization of FRABIN and SNX3 in the S16 rat SC line by immunofluorescence. We noticed vesicular staining of the endosomal marker SNX3, as previously described by Xu *et al.*,³⁸ and colocalization with FRABIN, especially at the perinuclear region (Fig. 5A). In

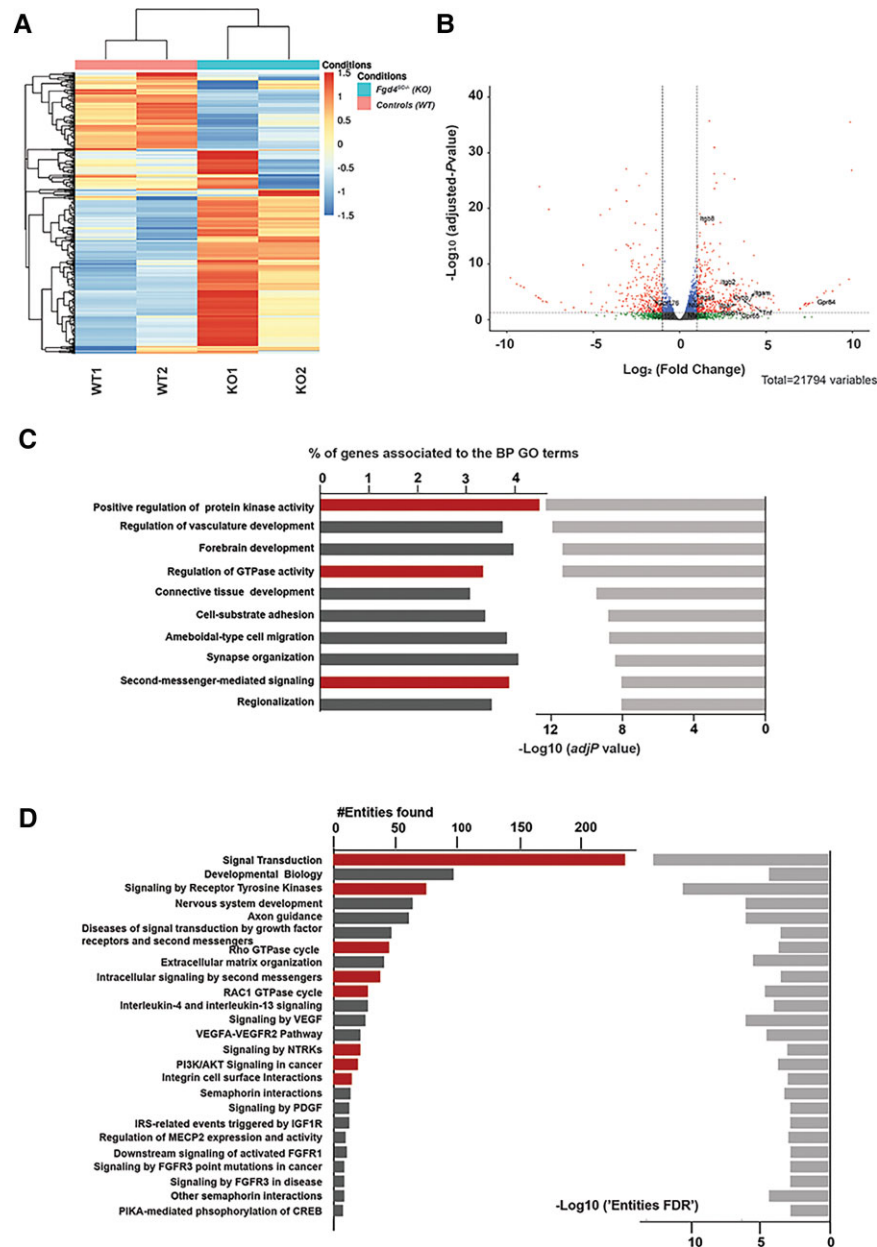


Figure 3 Transcriptional profiles of *in vitro* myelin samples (DRG/SC co-cultures) from conditional knockout (*Fgd4^{SC-/-}*) and control (WT) mice. (A) Full heat map of unsupervised hierarchical clustering of the four samples ($n = 2$ replicates for *Fgd4^{SC-/-}* and 2 replicates for WT). The scale bar unit is obtained applying a variance stabilizing transformation to the count data (DESeq2: VarianceStabilizingTransformation) before normalization. (B) Volcano plots showing the distribution of gene expression fold changes and adjusted P-values between the two conditions. A total number of 21 794 genes were tested. $P_{adj} < 0.05$ was used as the threshold to reject the null hypothesis and consider the difference in gene expression. Red plots represent significantly deregulated genes [adjusted P-value < 0.05, with fold change (FC) > 2 or < -2]. Genes with significant deregulation (adjusted P-value < 0.05) but with small FC (-2 < FC < 2) are indicated in blue. Green and grey dots represent genes with non-significant fold changes (adjusted P > 0.05). (C) Top 10 BP GO terms enriched in the DEGs. We identified BPs with an adjusted P-value lower than 0.05. The bars on the left represent the percentage of DEGs determined for each represented GO term from the total number of DEGs. Light grey bars on the right represent the enrichment score (-Log₁₀ of adjusted P-value) for each GO term. GO terms with particularly interesting functions, regarding the NRG1 type III pathway and FRABIN, are highlighted in red. (D) Top 25 reactome pathways enriched for the 536 genes found in the top 10 significantly enriched GO terms from C (adj. P-value < 0.001). The bars represent the number of DEGs found in each reactome pathway. Pathways with particularly interesting functions regarding the NRG1 type III pathway and FRABIN are highlighted in red.

parallel, we evaluated their potential interaction by co-immunoprecipitation. HEK293 cells previously transfected with FRABIN-His-V5 were subjected to immunoprecipitation using an anti-V5 antibody. Western blot analysis revealed that SNX3 was co-immunoprecipitated in the lysate fraction (Fig. 5B and Supplementary Fig. 6A).

We then examined the levels of SNX3 in control and knockout conditions, by western blot, *in vitro* and *in vivo*. We observed a significant increase in the levels of expression of SNX3 in *Fgd4^{SC-/-}* co-cultures as well as in the sciatic nerves of *Fgd4^{SC-/-}* animals in comparison to controls (Fig. 5C-F and Supplementary Fig. 6D and E). To determine whether the

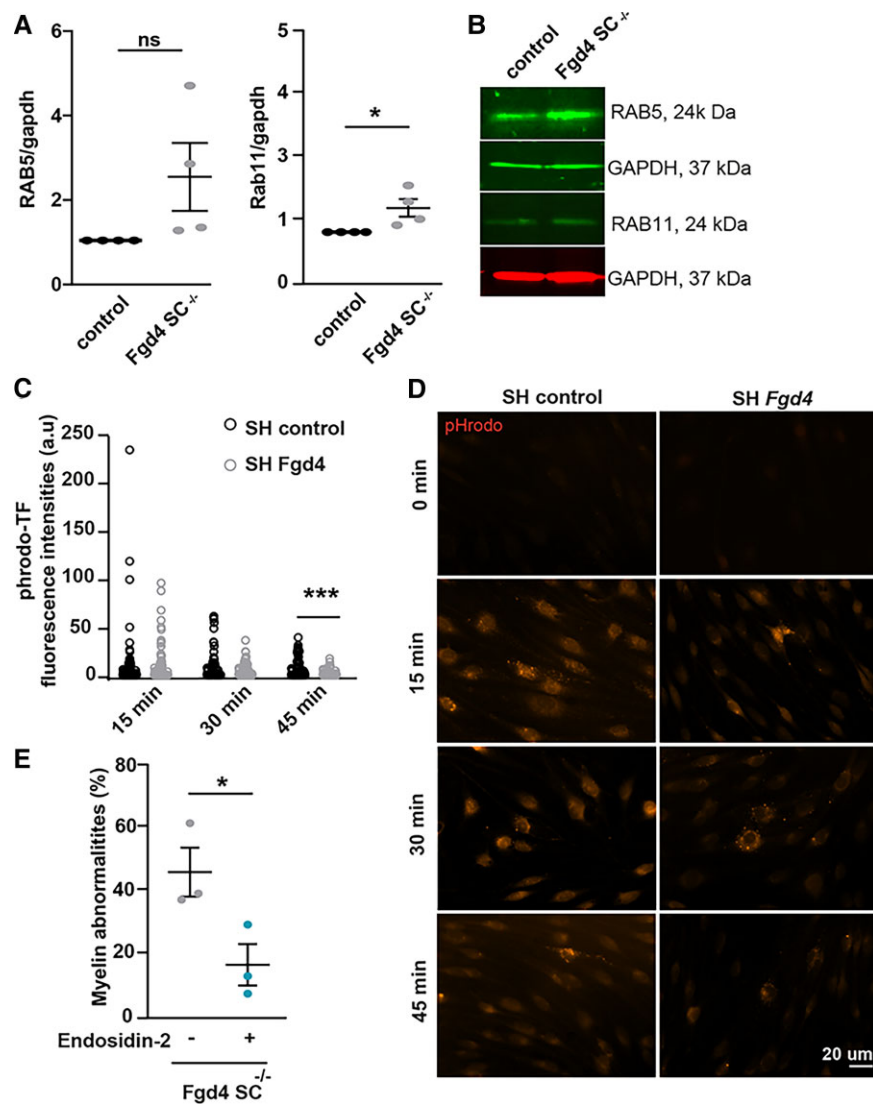


Figure 4 Altered endocytic trafficking contribute to the abnormal myelination observed in *Fgd4*^{SC-/-} conditions. (A and B) Expression of two endosomal markers (i.e. RAB5: early endosome and RAB11: recycling endosome) in *Fgd4*^{SC-/-} co-cultures: RAB11 is significantly upregulated in *Fgd4*^{SC-/-} co-cultures as compared to control (A). Quantification of RAB5 and RAB11 expression levels in western blot observed in B. Data are expressed as mean \pm SEM ($n = 3$ co-cultures) and normalized to the control values. Statistical analysis: unpaired Student's *t*-test. (B) Illustration of RAB5 and RAB11 expression patterns observed by western blot in control and *Fgd4*^{SC-/-} co-cultures. (C and D) pHrodo-Transferrin (pHrodo-TF) trafficking is altered in primary SCs infected with a Lv expressing a shRNA control or directed against *Fgd4*. After Lv infection (48 h), SCs were incubated with pHrodo-TF during 15, 30 or 45 min and immediately fixed in PFA 4%. pHrodo-TF is weakly fluorescent at a neutral pH, but brightly fluorescent in acidic compartments such as endosomes. (C) pHrodo-TF fluorescence was quantified in infected cells ($n = 60$ – 80 cells for each condition, from three independent cultures) and data are represented as individual values for each time point. Statistical analysis: unpaired Student's *t*-test for each time point. (D) Examples of pHrodo-TF labelling after 0, 15, 30 or 45 min in control (shRNA-control) and knocked-down (shRNA-*Fgd4*) conditions. (E) The blocking of endosomal recycling using Endosidin-2 (1 μ M) reduces significantly the proportion of abnormal myelin in *Fgd4*^{SC-/-} co-cultures compared to non-treated conditions. Data are expressed as mean percentage \pm SEM ($n = 3$ co-cultures). Statistical analysis: unpaired Student's *t*-test. * $P < 0.05$, ** $P < 0.01$, *** $P < 0.001$.

upregulation of SNX3 was contributing to CMT4H pathology, we downregulated the expression of SNX3 using RNA interference in *Fgd4*^{SC-/-} co-cultures. *Fgd4*^{SC-/-} co-cultures were infected with Lv expressing either a control shRNA or two different shRNAs targeting *Snx3*. The efficiency of SNX3 KD was evaluated 1 week post-infection by western blot (Supplementary Fig. 3A and B and Supplementary Fig. 6M). By quantifying the number of MBP+ segments harbouring myelination abnormalities, we noticed a significant reduction in their percentage following *Snx3* KD in *Fgd4*^{SC-/-} co-cultures with a KD of *Snx3*: $36.5\% \pm 1.9$ in *Fgd4*^{SC-/-} co-cultures + Lv-SH control, $22.7\% \pm 1.3$ in *Fgd4*^{SC-/-}

co-cultures + Lv-SH SNX3-1, or $17.8\% \pm 1.6$ in *Fgd4*^{SC-/-} co-cultures + Lv-SH SNX3-2 (Fig. 5G). We conclude that SNX3 is a partner of FRABIN in SCs and that an increase in SNX3 levels is likely to contribute to the focal hypermyelination events in CMT4H (Supplementary Fig. 4).

Niacin reduces myelin abnormalities in both *in vitro* and *in vivo* models of CMT4H

It is known that the amount of axonal NRG1-type III, and its downstream signalling via the activation of the ERBB2/3 receptors,

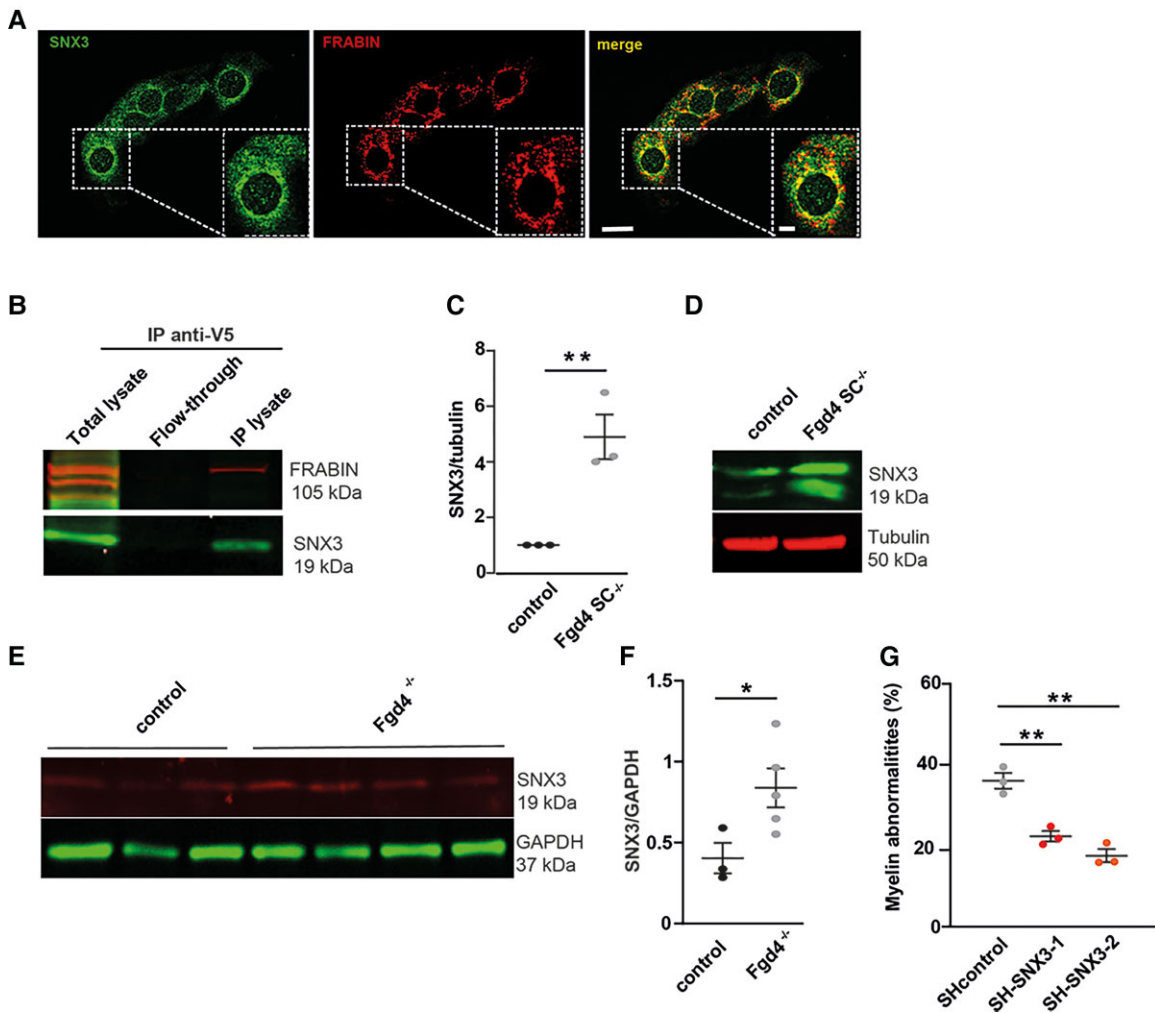


Figure 5 SNX3, a new partner of FRABIN, contribute to abnormal myelination *in vitro*. (A) FRABIN (red) colocalizes with the endosomal marker SNX3 (green) in the immortalized S16 rat SC line. Colocalization areas are visualized in yellow in the merge picture. Scale bar of the whole picture = 20 μm , scale bar of the enlarged picture = 10 μm . (B) Co-immunoprecipitation (IP) of SNX3 and FRABIN in HEK293 cells overexpressing V5-tagged FRABIN. SNX3 was detected using an anti-SNX3 antibody after immunoprecipitation of V5-FRABIN using an anti-V5 antibody. Note that both FRABIN and SNX3 are found only in the IP lysate, and not in the flow-through fraction. (C and D) SNX3 levels are increased in *Fgd4*^{SC-/-} co-cultures. SNX3 levels of expression were evaluated by western blot in both control and *Fgd4*^{SC-/-} co-cultures. (C) Quantification of proteins levels of SNX3 observed by western blot in co-cultures. Data are expressed as mean \pm SEM ($n = 3$ co-cultures) and normalized to the control values. Statistical analysis: unpaired Student's t-test. (D) Western blot illustration of SNX3 expression profile, normalized to tubulin. (E and F) SNX3 levels are increased in sciatic nerves from knockout CMT4H animals (*Fgd4*^{-/-}). SNX3 levels of expression were evaluated by western blot in sciatic nerves from 1-year-old *Fgd4*^{-/-} and control mice. (E) Quantification of protein levels of SNX3 observed by western blot in 1-year-old *Fgd4*^{-/-} and control's sciatic nerves. Data are expressed as mean \pm SEM ($n = 3$ controls and $n = 5$ *Fgd4*^{-/-}). Statistical analysis: unpaired Student's t-test. (F) Western blot illustration of SNX3 expression profile, normalized to GAPDH. (G) Knockdown of *Snx3* reduces significantly the number of myelin abnormalities in *Fgd4*^{SC-/-} co-cultures. *Fgd4*^{SC-/-} co-cultures were infected at Day 1 after plating with Lv expressing either SH control, or SH-SNX3 (1 and 2). Myelination was then induced by ascorbic acid (50 μM) treatment over 12 days. Data are expressed as mean \pm SEM ($n = 3$ co-cultures). Statistical analysis: one-way ANOVA, with Sidak post hoc test (multiple comparison to SH control). * $P < 0.05$, ** $P < 0.01$, *** $P < 0.001$.

determines the thickness of myelin sheath.^{10,11} Also, nerves from patients affected with CMT4H, due to loss of function mutations in FRABIN, display abnormalities characteristic of aberrant hypermyelination, such as outfoldings.^{5,7-9} Here we showed that this abnormal myelination observed in the absence of FRABIN is due to abnormal regulation of the NRG1 type III/ERBB2/3 pathway (Fig. 2 and Supplementary Fig. 4). We therefore aimed at lowering myelination by reducing the NRG1 type III/ERBB2/3 signalling using nicotinic acid (niacin). Indeed, niacin has been shown to promote the activation of the α -secretase TACE, which leads to a shorter cleaved form of NRG1-type III unable to link its ERBB2/3 receptors.⁴⁰ Therefore, cleavage of NRG1 type III by TACE negatively regulates

PNS myelination. We first tested niacin treatment *in vitro* by adding 5 mM of niacin, concomitantly to ascorbic acid, every 2 days over 10 days, in *Fgd4*^{SC-/-} co-cultures. We observed that niacin treatment reduces by $\sim 60\%$ the number of myelin defects (*Fgd4*^{SC-/-}: 71.4% \pm 4.4 versus *Fgd4*^{SC-/-} + niacin: 28.4% \pm 4.6; Fig. 6A and B). We then checked, by western blot, whether the benefit of niacin treatment was due to a downregulation of NRG1 type III/Erbb2/3 signalling. After niacin treatment, we observed a significant reduction of the levels of expression of P-ErbB2 and ErbB2 (Fig. 6C and D and Supplementary Fig. 6I and J).

We then evaluated the myelination status of the sciatic nerves of niacin-treated *Fgd4*^{SC-/-} mice compared with saline-injected

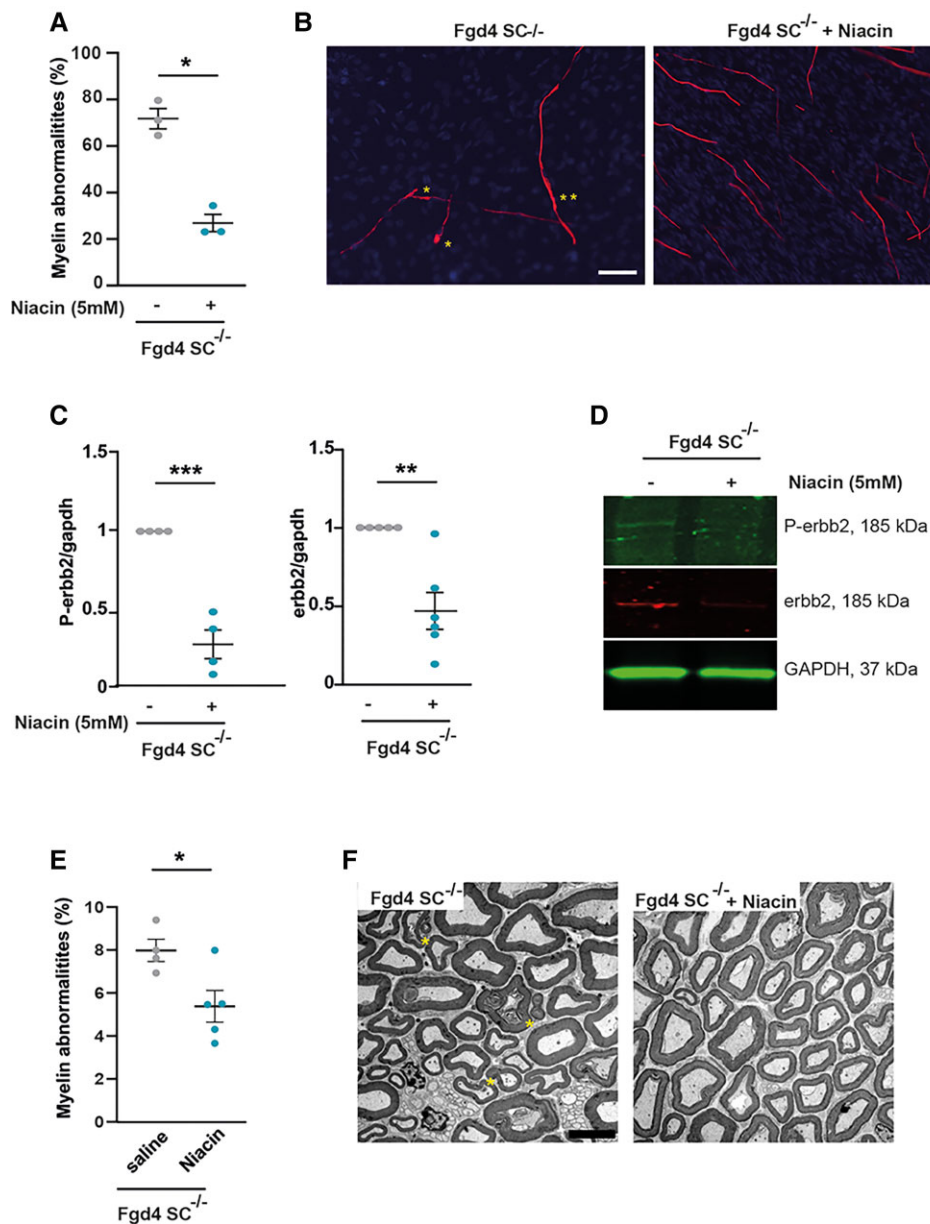


Figure 6 Downregulating NRG1-type III/ERBB2/3 signalling using niacin reduces myelination defects both *in vitro* and *in vivo*. (A and B) Niacin treatment reduces significantly myelin abnormalities in *Fgd4*^{SC-/-} co-cultures. *Fgd4*^{SC-/-} co-cultures were treated every 2 days with niacin (5mM) concomitantly to ascorbic acid addition (50 μ M) over 12 days. (A) Quantification of the myelin abnormalities. Data are expressed as mean \pm SEM ($n=3$ co-cultures) and normalized to the control values. Statistical analysis: unpaired Student's t-test. (B) Examples of MBP immunostaining in *Fgd4*^{SC-/-} co-cultures treated (right) or non-treated (left) with niacin. Examples of myelin abnormalities are indicated by asterisks (*outfolding, **tomacula). (C and D) Niacin treatment leads to a downregulation of the NRG1-type III/ERBB2/3 signalling pathway. P-ERBB2 and ERBB2 expression levels were assessed by western blot in non-treated and niacin-treated *Fgd4*^{SC-/-} co-cultures. (C) Quantification of P-ERBB2 and ERBB2 protein levels. Data are expressed as mean \pm SEM ($n=3$ co-cultures). Statistical analysis: unpaired Student's t-test. (D) Western blot pictures illustrating the expression of the markers described in C. (E and F) Niacin treatment reduces the proportion of abnormal myelin fibres *in vivo*. One-month-old *Fgd4*^{SC-/-} mice were daily injected with saline solution or niacin (60 mg/kg) over 8 weeks. Myelin abnormalities were quantified in the distal part of the sciatic nerves of the mice. (E) Quantification of the myelin abnormalities in sciatic nerves of treated and non-treated *Fgd4*^{SC-/-} mice. Data are expressed as mean \pm SEM ($n=4$ saline-treated animals and 5 niacin-treated animals). Statistical analysis: unpaired Student's t-test. * $P < 0.05$, ** $P < 0.01$, *** $P < 0.001$ (F) Electron microscopy pictures illustrating myelination of sciatic nerves of saline-treated (left) and niacin-treated *Fgd4*^{SC-/-} (right) mouse. Asterisks indicate outfolding. Scale bar = 5 μ m.

Fgd4^{SC-/-} mice. As we observed a significant proportion of myelin defects as soon as 3 months of age in *Fgd4*^{SC-/-} mice, mice were treated via IP injections for 8 weeks starting from 4 weeks of age (before the onset of myelin defects). Importantly, we noticed a significant reduction of the number of defective myelin fibres in treated versus

non-treated animals (*Fgd4*^{SC-/-} + niacin: 5% \pm 0.7 versus non-treated *Fgd4*^{SC-/-}: 7.4% \pm 0.5; Fig. 6E and F).

These observations demonstrate that the overactivation of the NRG1 type III/ERBB2/3 pathway underlies the myelination anomalies linked to CMT4H pathogenesis. Consequently, reducing NRG1

type III/ERBB2/3 NRG1 activation via niacin represents an interesting treatment perspective for CMT4H.

Discussion

CMT4H is an autosomal recessive demyelinating subtype of CMT disease, which we first described in 2005,⁵ and for which we, and others, described *FGD4* as the culprit gene in 2007.^{6,7} One distinctive feature of CMT4H is the presence in the nerves of patients of recurrent loops of myelin, called outfoldings.^{5,7-9,41,42} These rare myelination abnormalities have also been reported in other autosomal recessive demyelinating subtypes of CMT, i.e. CMT4B1 (OMIM #601382), CMT4B2 (OMIM #604563) and CMT4F (OMIM #614895), linked to mutations, respectively, in *MTMR2* (OMIM #603557), *SBF2/MTMR13* (OMIM #607697) and *PRX* (OMIM #605725), suggesting common pathophysiological mechanisms originating from an initial SC defect.^{31,43,44} Here, we sought to investigate these mechanisms by using both *in vitro* and *in vivo* models of CMT4H disease. Indeed, we generated a conditional knockout mouse model, with specific ablation of *Fgd4/FRABIN* in SCs, that we call *Fgd4^{SC-/-}* and from which we derived our *in vitro* myelin model based on DRG/SC co-cultures. We showed that the loss of *Fgd4/FRABIN* in SCs was sufficient to reproduce, both *in vitro* and *in vivo*, the characteristic myelin defects (i.e. outfoldings) observed in the nerves of CMT4H patients. *In vivo*, we detected the presence of those myelin abnormalities in the sciatic nerves of *Fgd4^{SC-/-}* animals, as early as 3 months of age, and showed that their proportion progressively increase over time. Our results agree with previous data observed in another CMT4H mouse model, using a different promoter (*Dhh*) to drive Cre recombinase expression in SCs.²¹ In our *Fgd4^{SC-/-}* model, we also provided, for the first time, evidence of secondary axonal degeneration reflected by late muscle denervation of the gastrocnemius of 12-month-old mutant mice, a phenomenon previously described in various *de-/dysmyelinating* CMT.^{45,46} Gait tests revealed that *Fgd4^{SC-/-}* mice display late motor impairment (i.e. at 18 months), resulting in the decrease of the pressure exerted by forepaws. These defects may reflect foot misplacement and deformation, as well as distal muscle weakness and amyotrophy observed in CMT4H patients.⁵ Overall, we showed that our *Fgd4^{SC-/-}* mouse model mimics most of the pathogenic features of CMT4H and is a reliable tool to study the molecular mechanisms underlying CMT4H-related aberrant myelination.

In this model and the derived *in vitro* myelin model, we showed that the observed myelination defects were connected to a dysregulation of the axo-glial NRG1 type-III/ERBB2/3 pathway and its downstream effectors, P-AKT and mTOR. Notably, we noticed a strong upregulation of P-ERBB2, P-AKT and mTOR in the *Fgd4^{SC-/-}* co-cultures and of ERBB2, and mTOR in the sciatic nerves of the full knockout *Fgd4^{-/-}* mice. In the PNS, it is known that the amount of axonal NRG1 type III, and its downstream signalling via the activation of the ERBB2/3 receptors and downstream effectors AKT and mTOR,³⁴ determines the thickness of the myelin sheath.^{10,11} Previous work from Bolino et al.¹³ in models of aberrant focal hypermyelination suggested that the upregulation of this signalling pathway is likely to contribute to the hypermyelination process, including the generation of aberrant loops of myelin. Also, several studies reported that myelin outfoldings might arise from the over-activation of PI3K, AKT and mTOR kinases.^{12-14,47} Indeed, constitutive activation of AKT or mTORC1 in SCs results in increased thickness and aberrant myelin^{14,48,49} and the use of the mTORC1 inhibitor, rapamycin, ameliorates myelin outfoldings observed in a DRG/SC co-culture model of CMT4B1.⁵⁰

Intriguingly, here, the upregulation of the NRG1 type III/ERBB2/3/AKT/mTOR pathway and aberrant focal hypermyelination in *Fgd4^{SC-/-}* co-cultures is not correlated to the upregulation of myelin proteins. Indeed, neither the genes encoding structural myelin proteins, from compact (*Mpz*, *Pmp22*, *Mbp*, *Pmp2*) and non-compact (*Gjb1*, *Mag*, *Prx*) myelin, nor the transcription factors regulating their expression (*Egr2*, *Sox10*) were found upregulated in *Fgd4^{SC-/-}* co-cultures. Our results are in accordance with other recent studies,^{51,52} describing, in different mouse models, an increase in myelin thickness, due to an activation of the NRG1 type III/ERBB2/3 pathway, independently of a change in the expression in the most common myelin genes or the master *Egr2* transcription factor. Although NRG1 type III/ERBB2/3 interaction promotes myelination by stimulating three canonical signalling pathways (PI3K/AKT/mTOR, MAPK/ERK and CaN/NFATc4),^{48,51} which are thought to converge on the activation of EGR2/KROX20, our results provide further evidence that the activation of the NRG1 type III/ERBB2/3 pathway and its downstream effectors (here PI3K/AKT/mTOR) can lead to enhanced production of myelin independently of the master myelin gene transcription factor *Egr2*.

Other downstream NRG1 type III/ERBB-dependent mechanisms might cause the increase in myelin thickness in CMT4H, such as the spatiotemporal regulation of small GTPases regulating actin dynamics (e.g. RAC1 or CDC42) to increase membrane spreading and motility around the axons⁵³ or else the regulation of cholesterol biosynthesis.⁵⁴ Interestingly, our RNA-Seq data show increased transcript levels of the transcription factor *Maf* in *Fgd4^{SC-/-}* conditions. Kim et al.³³ showed that *Maf* is activated following NRG1/ERBB2 signalling and has a crucial role in PNS myelination through the regulation of cholesterol biosynthesis,³³ a major constituent of myelin membranes. We were not able to confirm this upregulation, at the protein level, in sciatic nerves from 1-year-old *Fgd4^{-/-}* mice, which may due to the late myelination stage at which we tested its expression. Indeed, *Maf* expression is strongly induced during the early phase of SC myelination and its ablation leads to hypomyelination. Our results suggest that Frabin has a role in the transduction of signals regulating cholesterol biosynthesis in SCs and might help to understand how NRG1 type III/ERBB2/3 coordinates myelin protein production and cholesterol synthesis in these cells.

Moreover, our transcriptomic data did not reveal any changes of expression in the NRG1 type III/ERBB2/3 signalling pathway in *Fgd4^{SC-/-}* co-cultures, suggesting a regulation of those proteins at the protein level. In our case, we noticed a significant increase in the protein levels of ERBB2 and P-ERBB2 but not of NRG1 type III, showing that the loss of *Fgd4/FRABIN* in SCs may upregulate specifically ERBB2 levels rather than NRG1 type III itself. Indeed, emerging evidence indicates that ERBB receptor signalling is regulated by endocytic trafficking that controls its degradation or recycling towards the plasma membrane.^{15,55-57} Interestingly, previous work by Horn and colleagues²¹ has shown that the downregulation of *Fgd4/FRABIN* in a rat SC line impairs the endocytosis of the transferrin receptor (*Tfrc*). Here, by performing transferrin uptake assays, we demonstrate that the downregulation of *Fgd4/FRABIN* in primary SC do not affect the basal level of *Tfrc*'s endocytosis but rather promotes its recycling back to the membrane. In *Fgd4^{SC-/-}* co-cultures, we also observed the upregulation of the small GTPase RAB11, which regulates the trafficking of cargoes to the endocytic recycling compartment for direct recycling to the plasma membrane.⁵⁸

In our RNA-Seq data, we also noticed an increase in the levels of the *Rab11fip2* transcript in *Fgd4^{SC-/-}* co-cultures. *Rab11fip2* encodes an effector of Rab11, member of the Rab11-family interacting

proteins,^{59,60} which link endocytic vesicles with cytoskeletal motors for transport of cargoes along actin and microtubules and regulate the balance of transport on these two filament types.³⁶ Although we were not able to confirm this deregulation at the protein level due to a lack of specificity of the antibodies used to detect Rab11FIP2, this result further supports the fact that altered endosomal recycling is a key mechanism underlying CMT4H pathophysiology. Indeed, in *Fgd4*^{SC-/-} co-cultures, we showed, for the first time, that slowing down endosomal recycling using ES2 decreases significantly the proportion of abnormal myelinated segments.

Our data support the fact that FRABIN, through binding to PIs, regulates the endocytic trafficking of cargo proteins, such as ERBB receptors. Consequently, the enhancement of NRG1 type III/ERBB2/3 signalling observed in our models could be due to accelerated recycling of the ERBB2 receptor towards the SC plasma membrane, rather than to increased ERBB2 production. The upregulation of *Erbin*, observed in our RNA-Seq data in *Fgd4*^{SC-/-} co-cultures and confirmed in sciatic nerves from 1-year-old *Fgd4*^{-/-} mice, further strengthens this hypothesis of altered ERBB2 trafficking and recycling in CMT4H. Indeed, ERBIN, through interaction with ERBB2, is implicated in the stabilization and internalization of the ERBB2 protein.³⁴ Importantly, deletion of *Erbin* enhances ERBB2 internalization and degradation and leads to hypomyelination of mouse peripheral nerves. Conversely, the upregulation of *Erbin* observed here in *Fgd4*^{SC-/-} co-cultures and *Fgd4*^{-/-} sciatic nerves, is likely to reduce ERBB2 degradation and increase its levels at the membrane, hence causing hypermyelination.

Finally, by Y2H experiments, we identified for the first time the Sorting Nexin 3 (SNX3) protein, as a partner of FRABIN in the PNS. SNX3 belongs to the Sorting Nexins (SNXs) family of PI-binding proteins⁶¹ and is associated with early endosomes through its PX domain. Most interestingly, we observed that SNX3 is strongly upregulated in conditions of loss of *Fgd4*/FRABIN and conversely, that downregulation of *Snx3* using shRNA, in *Fgd4*^{SC-/-} co-cultures, reduces the aberrant myelination, typical of the disease. Accumulating evidence suggests that SNX proteins, in addition to binding to membranes play a critical role in cargo selection.⁶² Interestingly, modulation of SNX3 expression has been reported to alter the delivery of Tfrc to recycling endosomes.^{38,39} Moreover, SNX3 has been recently identified as a novel regulator, independent of the retromer complex, mediating tubular endosomal recycling of clathrin-independent endocytosis,⁶³ the mechanism by which ERBB2 and ERBB3⁶⁴ are internalized,⁶⁵ and which is likely to implicate actin remodelling and RhoGTPases.⁶⁶

The fate and sorting of cargoes packaged in vesicles of the endolysosomal system rely greatly on the heterogeneity of vesicles' membranes, variously enriched in different PIs that help to shape compartmental identity.²⁰ Importantly, FGD4/FRABIN, in addition to one F-actin binding domain and the RhoGEF domain, has two PH domains with binding specificity to PI(3,4,5)P3, PI(4,5)P2 and PI(3,4)P2 and one FYVE domain with binding specificity to PI(3)P.^{6,67} This specific protein structure, together with the demonstrated interaction with SNX3, strongly suggests that FRABIN could play a major role in orchestrating ERBB2 trafficking and hence the activated signalling cascades downstream from NRG1 type III/ERBB2/3 interaction. Although additional experiments are required to identify all actors and steps involved in the pathomechanisms underlying CMT4H, the results of our RNA-Seq experiments point out integrin signalling as an important downstream deregulated pathway. Interestingly, in CMT4C, SH3TC2 associates with the laminin receptor, integrin- α 6 and aberrant Rab11-dependent endocytic trafficking of this integrin is thought to be involved in the

demyelination seen in patients' nerves.⁶⁸ Like RAB11FIP2, SH3TC2 is a Rab11 effector.⁶⁹ It also interacts with ERBB2/3 after its activation at the plasma membrane⁷⁰ and plays a role in ERBB2/3 receptor internalization and/or intracellular trafficking. Therefore, it is tempting to speculate that SH3TC2 could be implicated in the defective ERBB receptor trafficking observed here in CMT4H and might act synergistically or antagonistically with FRABIN to regulate the activation of NRG1 type III/ERBB2/3 downstream effectors by targeting them to particular endocytosis compartments.

Overall, our results point to defective endosomal recycling as one main cause of the aberrant myelination associated with the loss of *Fgd4*/FRABIN. Among other genes responsible for autosomal recessive demyelinating CMT, beyond SH3TC2 (CMT4C, OMIM #601596), MTMR2 (CMT4B1, OMIM #601382) has also been reported to regulate endocytic trafficking. All three genes (*FGD4*, *SH3TC2*, *MTMR2*) encode proteins which are connected to defects in endocytic signalling.^{13,70–72} This suggests that defective endocytic trafficking and NRG1 type III/ERBB2/3 pathway is a key common pathogenic mechanism for these forms of CMT and a potential common treatment for those CMTs.

Interestingly, previous work in models of CMT4B1 showed that treatment with niacin efficiently restored proper myelination. Nicotinic acid/niacin is a compound known to enhance TACE activity⁷³ and hence negatively regulates NRG1 type-III/ERBB2/3 signalling.¹³ Indeed, BACE-1 and TACE are known to cleave NRG1 type III at distinct cleavage sites, thereby regulating myelination either positively for BACE-1⁷⁴ or negatively for TACE.⁷⁵ Because we showed that the dysregulation of the NRG1 type-III/ERBB2/3 signalling pathway is a major contributor to aberrant myelination in CMT4H, we used niacin to assess its capacity to rescue myelin outfoldings in our models. Remarkably, the use of niacin improved myelination of both *Fgd4*^{SC-/-} co-cultures and animals' sciatic nerves.

Overall, our study provides new key insights into the pathophysiological mechanisms underlying CMT4H. We demonstrate that FRABIN plays a major role in PNS myelination by regulating the levels of NRG1 type III/ERBB2/3 signalling through accelerated recycling of the ERBB2 receptor towards the SC plasma membrane. By identifying SNX3 as a new interactor of FRABIN or new potential effectors of the deregulated pathways, such as ERBIN and MAF, we provide cues to understand how FRABIN contributes to proper ERBB2 trafficking or even myelin membrane addition through cholesterol synthesis.

Our results open new avenues for a better understanding and treatment of CMT4H as well as for other hypermyelinating neuropathies.

Acknowledgements

We thank the PiCSL-FBI core facility (IBDM, AMU-Marseille), member of the France BioImaging national research infrastructure, in particular Nicolas Brouilly, who performed the electron microscopy experiments. We are grateful to the Genomics and Bioinformatics facility (GBiM), namely Camille Humbert, Christel Castro, Nathalie Trévisiol and Catherine Aubert, from the U 1251/Marseille Medical Genetics laboratory, for performing RNA-Seq experiments and analysis. We thank Thomas Marissal for his help with the statistical analysis.

Funding

This research work was supported by the French Association against Myopathies (Association Française contre les Myopathies) grants: # MNH-Decrypt, # TRIM-RD and # MoTharD).

Competing interests

The authors declare that there is no conflict of interest.

Supplementary material

Supplementary material is available at *Brain* online.

References

- Skre H. Genetic and clinical aspects of Charcot–Marie–Tooth’s disease. *Clin Genet*. 1974;6:98–118.
- Harding AE, Thomas PK. The clinical features of hereditary motor and sensory neuropathy types I and II. *Brain*. 1980;103:259–280.
- Pareyson D, Scaioli V, Laura M. Clinical and electrophysiological aspects of Charcot–Marie–Tooth disease. Historical article review. *Neuromolecular Med*. 2006;8(1–2):3–22.
- Pipis M, Rossor AM, Laura M, Reilly MM. Next-generation sequencing in Charcot–Marie–Tooth disease: Opportunities and challenges. *Nat Rev Neurol*. 2019;15:644–656.
- De Sandre-Giovannoli A, Delague V, Hamadouche T, et al. Homozygosity mapping of autosomal recessive demyelinating Charcot–Marie–Tooth neuropathy (CMT4H) to a novel locus on chromosome 12p11.21–q13.11. *J Med Genet*. 2005;42:260–265.
- Delague V, Jacquier A, Hamadouche T, et al. Mutations in *FGD4* encoding the Rho GDP/GTP exchange factor FRABIN cause autosomal recessive Charcot–Marie–Tooth type 4H. *Am J Hum Genet*. 2007;81:1–16.
- Stendel C, Roos A, Deconinck T, et al. Peripheral nerve demyelination caused by a mutant Rho GTPase guanine nucleotide exchange factor, frabin/*FGD4*. *Am J Hum Genet*. 2007;81:158–164.
- Baudot C, Esteve C, Castro C, et al. Two novel missense mutations in *FGD4*/*FRABIN* cause Charcot–Marie–Tooth type 4H (CMT4H). *J Peripher Nerv Syst*. 2012;17:141–146.
- Boubaker C, Hsairi-Guidara I, Castro C, et al. A novel mutation in *FGD4*/*FRABIN* causes Charcot Marie Tooth disease type 4H in patients from a consanguineous Tunisian family. *Ann Hum Genet*. 2013;77:336–343.
- Michailov GV, Sereda MW, Brinkmann BG, et al. Axonal neuregulin-1 regulates myelin sheath thickness. *Science*. 2004;304:700–703.
- Taveggia C, Zanazzi G, Petrylak A, et al. Neuregulin-1 type III determines the ensheathment fate of axons. *Neuron*. 2005;47:681–694.
- Goebbels S, Oltrogge JH, Wolfer S, et al. Genetic disruption of Pten in a novel mouse model of tomaculous neuropathy. *EMBO Mol Med*. 2012;4:486–499.
- Bolino A, Piguet F, Alberizzi V, et al. Niacin-mediated Tace activation ameliorates CMT neuropathies with focal hypermyelination. *EMBO Mol Med*. 2016;8:1438–1454.
- Domenech-Estevéz E, Baloui H, Meng X, et al. Akt regulates axon wrapping and myelin sheath thickness in the PNS. *J Neurosci*. 2016;36:4506–4521.
- Lee SM, Chin LS, Li L. Dysregulation of ErbB receptor trafficking and signaling in demyelinating Charcot–Marie–Tooth disease. *Mol Neurobiol*. 2017;54:87–100.
- Markworth R, Bähr M, Burk K. Held up in traffic-defects in the trafficking machinery in Charcot–Marie–Tooth disease. *Front Mol Neurosci*. 2021;14:695294.
- Jiang LT, Chen YH, Huang JH, Tong WF, Jin LJ, Li LX. Aberrant neuregulin 1/*ErbB* signaling in Charcot–Marie–Tooth type 4D disease. *Mol Cell Biol*. 2022;42:e0055921.
- Ono Y, Nakanishi H, Nishimura M, et al. Two actions of frabin: Direct activation of *Cdc42* and indirect activation of *Rac*. *Oncogene*. 2000;19:3050–3058.
- Umikawa M, Obaishi H, Nakanishi H, et al. Association of frabin with the actin cytoskeleton is essential for microspike formation through activation of *Cdc42* small G protein. *J Biol Chem*. 1999;274:25197–25200.
- Cullen PJ, Carlton JG. Phosphoinositides in the mammalian endo-lysosomal network. *Subcell Biochem*. 2012;59:65–110.
- Horn M, Baumann R, Pereira JA, et al. Myelin is dependent on the Charcot–Marie–Tooth Type 4H disease culprit protein *FRABIN*/*FGD4* in Schwann cells. *Brain*. 2012;135:3567–3583.
- Feltri ML, D’Antonio M, Previtali S, Fasolini M, Messing A, Wrabetz L. *P0-Cre* transgenic mice for inactivation of adhesion molecules in Schwann cells. *Ann N Y Acad Sci*. 1999;883:116–123.
- Poitelon Y, Feltri ML. The pseudopod system for axon–glia interactions: Stimulation and isolation of Schwann cell protrusions that form in response to axonal membranes. *Methods Mol Biol*. 2018;1739:233–253.
- Dobin A, Gingeras TR. Mapping RNA-seq reads with STAR. *Curr Protoc Bioinformatics*. 2015;51:11.14.1–11.14.19.
- Tarasov A, Vilella AJ, Cuppen E, Nijman IJ, Prins P. Sambamba: Fast processing of NGS alignment formats. *Bioinformatics*. 2015;31:2032–2034.
- Pertea M, Pertea GM, Antonescu CM, Chang TC, Mendell JT, Salzberg SL. Stringtie enables improved reconstruction of a transcriptome from RNA-seq reads. *Nat Biotechnol*. 2015;33:290–295.
- Love MI, Huber W, Anders S. Moderated estimation of fold change and dispersion for RNA-seq data with DESeq2. *Genome Biol*. 2014;15:550.
- Benjamini Y, Hochberg Y. Controlling the false discovery rate: A practical and powerful approach to multiple testing. *J R Stat Soc*. 1995;57:289–300.
- Cohen J. *Statistical power analysis for the behavioral sciences*. 2nd ed. Routledge;1988;
- Field AP. *Discovering statistics using SPSS*. Sage Publications; 2005.
- Bolis A, Coviello S, Bussini S, et al. Loss of *Mtmr2* phosphatase in Schwann cells but not in motor neurons causes Charcot–Marie–Tooth type 4B1 neuropathy with myelin outfoldings. *J Neurosci*. 2005;25:8567–8577.
- Falls DL. Neuregulins: Functions, forms, and signaling strategies. *Exp Cell Res*. 2003;284:14–30.
- Kim M, Wende H, Walcher J, et al. *Maf* links Neuregulin1 signaling to cholesterol synthesis in myelinating Schwann cells. *Genes Dev*. 2018;32:645–657.
- Newbern J, Birchmeier C. *Nrg1*/*ErbB* signaling networks in Schwann cell development and myelination. *Semin Cell Dev Biol*. 2010;21:922–928.
- Prekeris R. Rabs, Rips, FIPs, and endocytic membrane traffic. *Sci World J*. 2003;3:870–880.
- Machesky LM. Rab11/FIP proteins link endocytic recycling vesicles for cytoskeletal transport and tethering. *Biosci Rep*. 2019;39:BSR20182219.
- Zhang C, Brown MQ, van de Ven W, et al. Endosidin2 targets conserved exocyst complex subunit EXO70 to inhibit exocytosis. *Proc Natl Acad Sci U S A*. 2016;113:E41–E50.
- Xu Y, Hortsman H, Seet L, Wong SH, Hong W. *SNX3* regulates endosomal function through its PX-domain-mediated interaction with *PtdIns(3)P*. *Nat Cell Biol*. 2001;3:658–666.
- Chen C, Garcia-Santos D, Ishikawa Y, et al. *Snx3* regulates recycling of the transferrin receptor and iron assimilation. *Cell Metab*. 2013;17:343–352.

40. Chen J, Cui X, Zacharek A, et al. Niaspan treatment increases tumor necrosis factor- α -converting enzyme and promotes arteriogenesis after stroke. *J Cereb Blood Flow Metab.* 2009;29:911-920.
41. Fabrizi GM, Taioli F, Cavallaro T, et al. Further evidence that mutations in FGD4/frabin cause Charcot-Marie-Tooth disease type 4H. *Neurology.* 2009;72:1160-1164.
42. Arai H, Hayashi M, Hayasaka K, Kanda T, Tanabe Y. The first Japanese case of Charcot-Marie-Tooth disease type 4H with a novel FGD4 c.837-1G>A mutation. *Neuromuscul Disord.* 2013;23:652-655.
43. Guilbot A, Delague V. De la souris à l'homme: La périaxine responsable d'une forme autosomale récessive de la maladie de Charcot-Marie-Tooth. *Medecine/sciences.* 2001;17:663-665.
44. Robinson FL, Niesman IR, Beiswenger KK, Dixon JE. Loss of the inactive myotubularin-related phosphatase Mtmr13 leads to a Charcot-Marie-Tooth 4B2-like peripheral neuropathy in mice. *Proc Natl Acad Sci U S A.* 2008;105:4916-4921.
45. Moss KR, Bopp TS, Johnson AE, Höke A. New evidence for secondary axonal degeneration in demyelinating neuropathies. *Neurosci Lett.* 2021;744:135595.
46. Previtali SC, Quattrini A, Bolino A. Charcot-Marie-Tooth type 4B demyelinating neuropathy: Deciphering the role of MTMR phosphatases. *Expert Rev Mol Med.* 2007;9:1-16.
47. Figlia G, Norrmen C, Pereira JA, Gerber D, Suter U. Dual function of the PI3K-Akt-mTORC1 axis in myelination of the peripheral nervous system. *eLife.* 2017;6:e29241.
48. Figlia G, Gerber D, Suter U. Myelination and mTOR. *Glia.* 2018;66:693-707.
49. Beirowski B, Wong KM, Babetto E, Milbrandt J. mTORC1 promotes proliferation of immature Schwann cells and myelin growth of differentiated Schwann cells. *Proc Natl Acad Sci U S A.* 2017;114:E4261-E4270.
50. Guerrero-Valero M, Grandi F, Cipriani S, et al. Dysregulation of myelin synthesis and actomyosin function underlies aberrant myelin in CMT4B1 neuropathy. *Proc Natl Acad Sci U S A.* 2021;118:e2009469118.
51. Belin S, Ornaghi F, Shackelford G, et al. Neuregulin 1 type III improves peripheral nerve myelination in a mouse model of congenital hypomyelinating neuropathy. *Hum Mol Genet.* 2019;28:1260-1273.
52. Scapin C, Ferri C, Pettinato E, et al. Enhanced axonal neuregulin-1 type-III signaling ameliorates neurophysiology and hypomyelination in a Charcot-Marie-Tooth type 1B mouse model. *Hum Mol Genet.* 2019;28:992-1006.
53. Sparrow N, Manetti ME, Bott M, et al. The actin-severing protein cofilin is downstream of neuregulin signaling and is essential for Schwann cell myelination. *J Neurosci.* 2012;32:5284-5297.
54. Quintes S, Goebbels S, Saher G, Schwab MH, Nave KA. Neuron-glia signaling and the protection of axon function by Schwann cells. *J Peripher Nerv Syst.* 2010;15:10-16.
55. Sorkin A, Goh LK. Endocytosis and intracellular trafficking of ErbBs. *Exp Cell Res.* 2008;314:3093-3106.
56. Tomas A, Futter CE, Eden ER. EGF Receptor trafficking: Consequences for signaling and cancer. *Trends Cell Biol.* 2014;24:26-34.
57. McLean JW, Wilson JA, Tian T, et al. Disruption of endosomal sorting in Schwann cells leads to defective myelination and endosomal abnormalities observed in Charcot-Marie-Tooth disease. *J Neurosci.* 2022;42:5085-5101.
58. Redpath GMI, Betzler VM, Rossatti P, Rossy J. Membrane heterogeneity controls cellular endocytic trafficking. *Front Cell Dev Biol.* 2020;8:757.
59. Hales CM, Griner R, Hobdy-Henderson KC, et al. Identification and characterization of a family of Rab11-interacting proteins. *J Biol Chem.* 2001;276:39067-39075.
60. Baetz NW, Goldenring JR. Rab11-family interacting proteins define spatially and temporally distinct regions within the dynamic Rab11a-dependent recycling system. *Mol Biol Cell.* 2013;24:643-658.
61. Teasdale RD, Collins BM. Insights into the PX (phox-homology) domain and SNX (sorting nexin) protein families: Structures, functions and roles in disease. *Biochem J.* 2012;441:39-59.
62. Wang J, Fedoseienko A, Chen B, Burstein E, Jia D, Billadeau DD. Endosomal receptor trafficking: Retromer and beyond. *Traffic.* 2018;19:578-590.
63. Tian Y, Kang Q, Shi X, et al. SNX-3 mediates retromer-independent tubular endosomal recycling by opposing EEA-1-facilitated trafficking. *PLoS Genet.* 2021;17:e1009607.
64. Reif R, Adawy A, Vartak N, et al. Activated ErbB3 translocates to the nucleus via clathrin-independent endocytosis, which is associated with proliferating cells. *J Biol Chem.* 2016;291:3837-3847.
65. Barr DJ, Ostermeyer-Fay AG, Matundan RA, Brown DA. Clathrin-independent endocytosis of ErbB2 in geldanamycin-treated human breast cancer cells. *J Cell Sci.* 2008;121:3155-3166.
66. Sandvig K, Kavaliuskiene S, Skotland T. Clathrin-independent endocytosis: An increasing degree of complexity. *Histochem Cell Biol.* 2018;150:107-118.
67. Kim Y, Ikeda W, Nakanishi H, et al. Association of frabin with specific actin and membrane structures. *Genes Cells.* 2002;7:413-420.
68. Vijay S, Chiu M, Dacks JB, Roberts RC. Exclusive expression of the Rab11 effector SH3TC2 in Schwann cells links integrin- $\alpha 6$ and myelin maintenance to Charcot-Marie-Tooth disease type 4C. *Biochim Biophys Acta.* 2016;1862:1279-1290.
69. Stendel C, Roos A, Kleine H, et al. SH3TC2, a protein mutant in Charcot-Marie-Tooth neuropathy, links peripheral nerve myelination to endosomal recycling. *Brain.* 2010;133:2462-2474.
70. Gouttenoire EA, Lupo V, Calpena E, et al. Sh3tc2 deficiency affects neuregulin-1/ErbB signaling. *Glia.* 2013;61:1041-1051.
71. Bolis A, Coviello S, Visigalli I, et al. Dlg1, Sec8, and Mtmr2 regulate membrane homeostasis in Schwann cell myelination. *J Neurosci.* 2009;29:8858-8870.
72. Lee HW, Kim Y, Han K, Kim H, Kim E. The phosphoinositide 3-phosphatase MTMR2 interacts with PSD-95 and maintains excitatory synapses by modulating endosomal traffic. *J Neurosci.* 2010;30:5508-5518.
73. Chen J, Cui X, Zacharek A, et al. Niaspan increases angiogenesis and improves functional recovery after stroke. *Ann Neurol.* 2007;62:49-58.
74. Hu X, Hicks CW, He W, et al. Bace1 modulates myelination in the central and peripheral nervous system. *Nat Neurosci.* 2006;9:1520-1525.
75. La Marca R, Cerri F, Horiuchi K, et al. TACE (ADAM17) inhibits Schwann cell myelination. *Nat Neurosci.* 2011;14:857-865.

1 **Supplementary Material and Methods**

3 **RT-PCR**

4 Total RNA was isolated from Wild Type (WT) and *Fgd4*^{SC-/-} mouse sciatic nerves using the
5 Purelink RNA Minikit (#12183018A₂, ThermoFisher Scientific, USA), following the
6 manufacturer's protocol. cDNA was generated using the SuperScript III one-step RT-PCR
7 (#12574018, ThermoFisher Scientific, USA) and random hexamers (#48190011,
8 ThermoFisher Scientific, USA). The deletion of exon 4 was detected by the amplification,
9 from cDNA, of a fragment between exons 3 and 7 of the *Fgd4* transcript, using the following
10 primers (*Fgd4*-mouse-3F: 5'- GAGTCTAATCCGGCCCCCTAC-3' and *Fgd4*-mouse-7R: 5'-
11 AAGGAATGGCGCCAACCTTTT-3').

13 **Behavioural gait test**

14 For the gait experiment, sex and age-matched *Fgd4*^{SC-/-} and WT littermates' mice were
15 monitored at 6 (n=9 WT and n=9 *Fgd4*^{SC-/-}), 12 (n=12 WT and n=13 *Fgd4*^{SC-/-}) and 18 (n=11
16 WT and n=13 *Fgd4*^{SC-/-}) months old. Gait was analyzed during spontaneous walk using an
17 automated gait analysis system (Gaitlab, Viewpoint, France). Before recording footprints,
18 mice were acclimated and trained to walk on the Gait system for two days. During the testing
19 session, a minimum of 2-3 completed runs were collected. We focused the analysis on
20 intensity-based parameters, paw-size as well as gait/posture, as previously described in¹.
21 Animals that did not complete at least 2 successful runs (stalling or reversing during gait,...)
22 were removed from the study.

24 **Electron microscopy and morphometric analysis**

25 The sciatic nerves were dissected and fixed in 2% ParaFormaldehyde (PFA) and 2.5%
26 Glutaraldehyde in 0.1M cacodylate buffer for 2 hours. The next day, the nerves were washed
27 three times in 0.1M cacodylate buffer and post-fixed in buffered 1% OsO₄ for one hour. After
28 washes in distilled water, the samples were contrasted in aqueous 1% uranyl acetate. Samples
29 were then dehydrated in graded series of ethanol baths (30 minutes each) and infiltrated with
30 epon resin in ethanol (1:3, 2:2, 3:1) for 2 hours for each, and finally in pure resin overnight.
31 The next day the nerves were embedded in fresh pure epon resin and cured for 48h at 60°C.
32 500 nm semi-thin and 70 nm ultra-thin sections were performed on a Leica UCT

33 Ultramicrotome (Leica, Austria). Semi-thin sections were stained with toluidine blue and
34 ultrathin sections were deposited on formvar-coated slot grids. The grids were contrasted
35 using uranyl acetate (10 minutes) and lead citrate (5 minutes) and observed using an FEI
36 Tecnai G2 at 200 KeV. The acquisition was performed on a Veleta camera (Olympus, Japan).
37 The proportion of fibers having out- and infoldings was counted on ten fields corresponding
38 to a range of 600-800 fibers for each sciatic nerve of at least three animals.
39 To perform g-ratio analysis, digitalized images of fiber semithin sections of the sciatic nerves
40 were obtained with a 100× objective of a phase-contrast microscope (BX59, Olympus). At
41 least ten images from three different animals per genotype at 3, 6, and 18 months old were
42 acquired. g-ratio analysis was performed on micrographs using Image J (National Institutes of
43 Health, Bethesda, MD) plug-in (g-ratio calculator) developed in collaboration with the
44 cellular imaging facility of the University of Lausanne and available at <http://cifweb.unil.ch>,
45 as previously described in Arnaud et al.2009 ².

46
47

48 **Immunohistochemistry**

49 Mice were sacrificed with an overdose of CO₂. Gastrocnemius muscles were dissected out
50 and fixed in 4 % PFA for 30 min. Samples were then incubated in 25 % sucrose solution at 4
51 °C for 24 h. Tissues were embedded in the Optimal Cutting Temperature compound
52 (#3801480, Leica, USA) and stored at -80 °C before processing. Embedded muscles were
53 then cut to twenty-five µm-thick sections, mounted on slides coated with Superfrost Plus
54 (#LSFPLUS, THERMO SCIENTIFIC MENZEL, USA). Muscle sections were incubated
55 overnight at 4 °C in blocking solution (2 % BSA, 10 % Normal Goat Serum, 0.1 % Triton and
56 PBS) with chicken anti-NFM (#822701, BioLegend, USA, previously #PCK-593P, Covance,
57 USA). Sections were next incubated with Goat anti-Chicken IgY (H+L) Secondary Antibody,
58 Alexa Fluor 488, (#ab150169, Abcam, UK) and α-Bungarotoxin, Alexa Fluor™ 555
59 conjugate (#B35451, thermofisher Scientific, USA), (1:500), and mounted in Duolink
60 mounting medium (#DU082040, Sigma-Aldrich, USA) . Neuromuscular junctions were
61 imaged on a Zeiss ApoTome.2 microscope (Zeiss, Germany) equipped with an AxioCam
62 MRm camera.

63

64 **Lentivirus infection**

65

66 Fgd4/FRABIN was either overexpressed or downregulated in WT DRG/SC cocultures or in
67 rat primary SC using Lentivirus vectors (Lv) designed and produced by the Vector builder
68 company (<https://en.vectorbuilder.com>, USA). For overexpression, we designed control Lv
69 (Lv-control) expressing EGFP under the CMV promoter and Lv allowing the expression of
70 mouse Fgd4 (Lv-Fgd4) under the CMV promoter. For the knockdown experiments, we used
71 an Lv expressing a shRNA against rat *Fgd4* previously validated in Horn et al. 2012³
72 (targeted sequence: 5'-GAAGAAGAGGATATTGTA-3') referred to as LvSHFgd4-GFP. Lv-
73 Shcontrol-GFP expressing a shRNA scramble, randomly produced, was provided by
74 Vectorbuilder (#VB151023-10034, Vectorbuilder, USA). Both Lv vectors express EGFP
75 under the CMV promoter, in addition to the shRNA, allowing tracing of the infected cells.
76 We used the same strategy to knockdown the *Snx3* gene in DRG/SC cocultures or in primary
77 SCs. Here, we used Lv expressing two shRNAs targeting *Snx3* (Sh-0: 5'-
78 GCCCAGAATGAACGTTGTCTT-3'; Sh-3: 5'-AGAGAGAGCAAGGTTGTAGTT-3'),
79 both provided by Sigma-Aldrich (USA). Cells (DRG/SC cocultures or primary SCs) were
80 infected with the described Lv at a dose of 15 TU/cell 24 h after plating.

81

82 **Transferrin assay**

83 Rat primary SCs were plated at a density of 50 000 cells per well and infected 24h later with
84 Lv-SHcontrol-GFP or SHFgd4-GFP (15 TU/cell). Two days after the infection, cells were
85 incubated with pHrodo-red Transferrin conjugate (#P35376, Thermofischer Scientific, USA)
86 at a dilution of 50µg/ml, for 30 min on ice, followed by 15, 30 or 45 min of incubation at 37
87 °C. After one PBS wash, cells were fixed in 4% PFA for 15 min. Samples were then mounted
88 in Duolink mounting medium (#DU082040, Sigma-Aldrich, USA) and pHrodo-TF
89 fluorescence intensities were visualized and captured on a Zeiss ApoTome.2 microscope
90 (Zeiss, Germany) equipped with an AxioCam MRm camera, with a 20 X objective. The
91 integrated density of fluorescence signal was analyzed only in the infected cells (*i.e.*, GFP+)
92 using ImageJ software.

93

94 **Cell lines and transfection**

95 HEK293 (Human embryonic kidney, # CRL-1573) and S16 rat SC (#CRL-2941) lines were
96 both provided by ATCC (Manassas, Virginia, USA). HEK293 and S16 cells were cultured in
97 DMEM (#41965, Thermofisher Scientific, USA) complemented with 10 % of FBS (#15000-
98 036, Thermofisher, USA) and 1 % of penicillin/streptomycin (#15070063, Thermofisher

99 Scientific, USA). To overexpress hFGD4/FRABIN in HEK293 cells, the pEx-FGD4-His-V5
100 vector was generated by Gateway cloning technology (ThermoFischer Scientific, USA).
101 Transfection experiments were performed using promofectin reagent (#PK-CT-2000-50,
102 PromoCell GmbH, Germany). Briefly, 300000 cells were seeded and transfected with 4µg of
103 plasmid following the manufacturer's recommendation. For immunoprecipitation, cells were
104 harvested 72 h post-transfection.

105

106 **Plasmids**

107 The plasmids used for the yeast-two hybrid experiment (pENTR-FL-hFGD4) and transfection
108 studies (pEx-FGD4-His-V5) were generated using Invitrogen Gateway cloning technology
109 (ThermoFischer Scientific, USA) following the manufacturer's instructions. Briefly, the entry
110 plasmid (i.e., pENTR-FL-hFGD4) was generated after the BP recombination reaction between
111 the *attB*-flanked hFGD4 fragment and the *attP*-containing donor vector pDONR221
112 (#12536017, ThermoScientific, USA) using the BP clonase enzyme kit (#11789013,
113 ThermoScientific, USA). The *attB*-flanked hFGD4 fragment was produced by PCR using the
114 "Expand High Fidelity Plus PCR System" (#3300226001, Roche, Switzerland) and the
115 following primers:

116 1F:5'GGGGACAAGTTTGTACAAAAAAGCAGGCTTCGAGGAAATTAACCTGCCTC
117 TGC3' and FGD4-GATEWAY-1R:
118 5'GGGGACCACTTTGTACAAGAAAGCTGGGTTCAGCATTCTGATTTTTTCTTAGG3'.

119 The expression vector pEx-FGD4-His-V5 was generated following an LR recombination
120 between the *attL* containing entry vector (pENTR-FL-hFGD4) and the *attR* destination vector
121 (pDEST40, #12274015, ThermoScientific, USA) using the LR Clonase enzyme mix
122 (#11791019, ThermoScientific, USA).

123

124 **Immunocytochemistry**

125 DRG/SC co-cultures were fixed with 4% PFA, washed in PBS, and then permeabilized for 5
126 minutes with methanol. After two PBS washes, cells were incubated 1-2 h in a blocking
127 solution (20% fetal bovine serum, 1% bovine serum albumin, 0.01% Triton in 1 X PBS) at
128 room temperature. Cells were then incubated with the following primary antibodies diluted in
129 the incubation solution overnight: chicken anti-neurofilament NF-M (1:1000) (#822701,
130 BioLegend, USA, previously #PCK-593P, Covance), rat anti-MBP (1:300) (#MAB386,
131 Merck-Millipore, Germany). After two washes in PBS, cells were incubated with one of the

132 following secondary antibodies: Donkey Anti-Rat IgG H&L (#150154, Alexa Fluor 555,
133 abcam, UK) (1:1000) and (#A21449, Goat Anti-Chicken IgY H&L (Alexa Fluor 647,
134 Invitrogen, USA) (1: 1000). Coverslips were then rinsed twice in PBS and mounted in a
135 duolink mounting medium (#DU082040, Sigma-Aldrich, USA) for microscope analysis.
136 Fluorescence images were captured with a Zeiss ApoTome.2 microscope (Zeiss, Germany)
137 equipped with an AxioCam MRm camera. Images were captured and merged with the ZEN
138 software (Zeiss, Germany) and were treated using ImageJ software.

139

140 **Protein extraction and Immunoblotting**

141 DRG/SC co-cultures or nerve samples were lysed in RIPA buffer supplemented with a
142 protease/phosphatase inhibitor cocktail (#78442, ThermoFisher Scientific, USA). The lysate
143 was passed through an 18–21-gauge needle and submitted to sonication using the Bioruptor
144 VCD-200 (Diagenode, Belgium). After centrifugation for 10 min at 20,000 x g at 4 °C, the
145 supernatant was removed and protein concentration was measured by use of a Bicinchoninic
146 acid (BCA) solution (#B9643-1LSigma-aldrich, USA) coupled to copper II sulfate solution
147 (#C2284-25ml, Sigma-aldrich, USA) following the manufacturer's recommendations. 40 µg
148 of samples' proteins were loaded on a Precast NuPage 4-12 % Bis-Tris gels (Thermofisher,
149 USA) and transferred onto a nitrocellulose membrane (GE healthcare life science, Germany).
150 The membrane was then blocked by incubation in blocking buffer (Intercept-blocking buffer,
151 Licor). The membrane was then incubated overnight with the following primary antibodies:
152 mouse anti-Neuregulin1 α / β 1/2 (D10) (1:500) (#sc-393009; Santa Cruz Biotechnology, USA),
153 rabbit anti-phospho-Akt (Ser473) (D9E) (1:2000) (#4060, Cell Signaling Technology, USA),
154 rabbit anti-Akt(pan) (C67E7) (1:1000) (#4691, Cell Signaling Technology, USA), rabbit anti-
155 HER2/ERBB2 (29D8) (1:1000) (#2165, Cell Signaling Technology, USA), rabbit anti-
156 phospho-HER2/ERBB2 (Tyr1248) (1:1000) (#2247, Cell Signaling Technology, USA), rabbit
157 anti-HER3/ERBB3 (1B2) (1:1000) (#4754, Cell Signaling Technology, USA), rabbit anti-
158 phospho-HER3/ERBB3 (Tyr1289) (D1B5) 1:1000) (#2842, Cell Signaling Technology,
159 USA), rabbit anti-rab11a (1:1000) (#ab65200, Abcam, UK), rabbit anti-rab5 (1:1000)
160 (#ab18211, Abcam, UK), rabbit anti-mTOR (7C10) (1:1000) (#2983T, Cell Signaling
161 Technology, USA), rabbit anti-SNX3 (1:300) (#ab56078, Abcam, UK), goat anti-gapdh
162 (1:1000) (#sc-48167, Santa Cruz Biotechnology, USA), rabbit anti-c-MAF (1:100)
163 (#ab77071, abcam, UK), rabbit anti-ERBIN (1:500) (#LSC47097, LSBio, USA), mouse anti-

164 tubulin (1:4000) (#T6074, Sigma-Aldrich, USA). After three final washes in 0.1 % PBS-
165 Tween 20, the membranes were incubated with secondary antibodies: IRDye® 800CW
166 Donkey anti-Rabbit IgG (H + L), IRDye® 680RD Donkey anti-Goat IgG (H + L), and
167 IRDye® 680RD Donkey anti-Mouse IgG (H + L) from Li-Cor Biosciences(USA), diluted at
168 1:10000. Membranes were then developed using the ChemiDoc imaging system from Biorad(
169 USA). Intensities of the bands were then analyzed using the ImageJ gel analyzer tool (ImageJ
170 Software, National Institute of Health, Bethesda, MD, USA, <http://rsb.info.nih.gov/ij>). A plot
171 profile of western blots was established, and the intensities of all bands were measured. For
172 each sample, the peak intensity was calculated for each target protein by dividing the target
173 protein intensity with the intensity of the loading control protein. Data were then normalized
174 to the control sample.

175

176

177 **Immunoprecipitation**

178 Co-immunoprecipitation (co-IP) experiments were performed using the Dynabeads Protein G
179 Immunoprecipitation Kit (#10007D, ThermoFisher Scientific, USA) following the
180 manufacturer's protocol. Briefly, HEK293 cells overexpressing His-V5-tagged human
181 FRABIN were washed with PBS 72 h post-transfection (with plasmid pEx-FGD4-His-V5),
182 and then incubated in a home-made lysis buffer (HEPES 50 mM, NaCl 150 mM, MgCl₂ 1.5
183 mM, EGTA 1 mM, Glycerol 10 %, Triton X100 0.1 %, protease inhibitor). First, 10ug of
184 primary mouse anti-V5 antibody (#ab27671, Abcam, UK) diluted in PBS-Tween 0.01% were
185 incubated with magnetic beads for 1h. The antibody-magnetic beads complex was then
186 incubated with the lysate containing 1 mg of proteins, overnight with end over end rotation.
187 The flow-through is then discarded after placing the tube containing the beads-antigen-
188 antibody lysate, on the magnet. Bound proteins were then eluted with elution buffer and
189 dissociated in 10 µl of NuPAGE LDS Sample Buffer (#NP0007, ThermoFisher Scientific,
190 USA). Samples were then boiled at 70 °C for 10 min before loading on a NuPage Bis-Tris
191 gel.

192

193 **Yeast two-hybrid (Y2H)**

194 GAL4-based yeast two-hybrid assay was performed, using a commercial human fetal brain
195 cDNA library containing cDNAs fused to the gal4 activation domain of pEXP-AD502
196 (ProQuest™, ThermoFisher Scientific, USA), as prey, and full length human *FGD4* cDNA as

197 a bait. To this purpose, the full-length coding sequence of *FGD4* (NM_139241) was
198 subcloned from the pENTR-FL-hFGD4, into a pDBA vector, using the Gateway technology
199 (Thermofisher Scientific, USA). The bait plasmid was transformed in MAV03 yeast strain
200 (MAT α ; leu2-3,112; trp1-901; his3 Δ 200; ade2-101; gal4 Δ ; gal80 Δ ;
201 SPAL10UASGAL1::URA3, GAL1::lacZ, GAL1::His3@LYS2, can1R, cyh2R) following the
202 previously described transformation protocol⁴. This bait did not show self-activation and was
203 further used for screening. MAV203 cells were then transformed with the prey cDNA library
204 as described⁴. Following transformation with the cDNA library, yeasts were plated onto
205 synthetic complete (SC) medium minus leucine (-L), minus tryptophane (-W), minus
206 histidine (-H) +25 mM 3-amino-1,2,4-triazole (3-AT) and, incubated at 30°C for 4–5 days.
207 Positive clones were patched onto SC-WHL + 3-AT in 96-well plates, incubated for 3 days at
208 30°C and transferred in liquid SC-WL for 3 days at 30°C with agitation to normalize the yeast
209 cell concentration used for the phenotypic assay. Cells were then diluted 1/20 in water,
210 spotted onto a selective medium (-WHL+25 mM 3-AT or -WUL), and incubated at 30°C for 4
211 to 5 days. To perform the β -galactosidase assay, undiluted yeast cells were spotted onto YPD
212 (yeast extract peptone dextrose) medium plates with nitrocellulose filters, and β -galactosidase
213 activity was evaluated one day after. Positive clones were sequenced by Sanger sequencing,
214 after PCR amplification using the following primers: forward: 5'-
215 CGCGTTTGGAAATCACTACAGGG-3' and reverse: 5'-
216 GGAGACTTGACCAAACCTCTGGCG-3'). The clones were identified by using BLAST.

217
218

219 **Legends to Supplementary Figures and Table**

220

221 **Supplementary Figure 1. *Fgd4*^{SC-/-} animals display normal myelination thickness of**
222 **sciatic nerves, but a late muscle denervation (A)** G-ratio analysis revealed no statistical
223 differences in myelin thickness in the sciatic nerves of 3, 6 and 18 mo WT and *Fgd4*^{SC-/-} mice.
224 A total of 500-1000 axons of diameter between 0.5 and 6 μ m were analysed (n=3 animals per
225 genotype). Data are represented as scatter plots of individual axons as a function of their
226 respective diameters determined at 3, 6 and 18 months old. Each point corresponds to one
227 fiber (gray points: *Fgd4*^{SC-/-} animals; black points: WT animals). **(B-C)** Late muscle
228 denervation observed in the gastrocnemius of *Fgd4*^{SC-/-} animals. Level of innervation of
229 gastrocnemius muscle evaluated by the colocalization of the neurofilament marker (NF-M)

230 and the acetylcholine receptor marker α -bungarotoxin in 12 months old WT (n=3) and
231 *Fgd4*^{SC-/-} (n=3) animals. Yellow asterisk indicate innervated NMJ, red asterisk indicate
232 denervated NMJ. Scale bar: 50 μ m. Statistical analysis: two-way repeated-measures ANOVA
233 (genotype*type of NMJs) with Sidak post-hoc test. Two-way ANOVA revealed a significant
234 difference on the proportion of the type of NMJs between WT and *Fgd4*^{SC-/-} conditions
235 (p=0.001). Sidak post hoc test show a significant increase in the proportion of denervated
236 NMJs in *Fgd4*^{SC-/-} compared to WT (p:0,01). **(D-E)** Levels of expression of cleaved and full-
237 length Neuregulin 1-type III (named respectively cNRG1 and fNRG1) were assessed by
238 western-blot analysis in *Fgd4*^{SC-/-} cocultures compared to control. **(D)** Data are expressed as
239 mean \pm sem (n=3-4 cocultures). Statistical analysis: unpaired Student's t-test. **(E)** Western
240 blot pictures illustrating the expression of the markers described in (D). **(F-G)** Levels of
241 expression of cNRG1 and fNRG1 were assessed by western-blot analysis in the sciatic nerves
242 of *Fgd4*^{-/-} mice compared to WT mice. **(F)** Data are expressed as mean \pm sem (n=3 animals
243 per genotype). Statistical analysis: unpaired Student's t-test. **(G)** Western blot pictures
244 illustrating the expression of the markers described in (E). * p<0.05, ** p<0.01, ***p<0.001.

245

246 **Supplementary Figure 2. Protein levels of ERBIN, but not MAF-1, are upregulated in**
247 **sciatic nerves from *Fgd4*^{-/-} knock-out mice .**

248 **(A-B)** Levels of expression of MAF-1 and ERBIN were assessed by western-blot analysis in
249 the sciatic nerves of 1 year old *Fgd4*^{-/-} mice. **(A)** Data are expressed as mean \pm sem (n=3
250 control and n=5 *Fgd4*^{-/-} animals). **(B)** Western blot pictures illustrating the expression of the
251 markers described in (A).

252

253 **Supplementary Figure 3. Effective knock-down of *Snx3* and *Fgd4/FRABIN* in vitro. (A-**

254 **B)** Lentivirus (Lv) expressing shRNA targeting *Snx3* lead to an efficient knock-down of *Snx3*
255 in primary rat SCs. Primary SCs were infected 1 day after plating with either Lv-SHcontrol,
256 LV-SH-SNX3-1 or 2, and harvested 7 days post-infection. Level of expression of SNX3 in
257 those conditions was evaluated by western-blot. **(C)** Knock-down of *Fgd4/FRABIN* in
258 primary SCs following Lv-shRNA targeting *Fgd4* and expressing GFP tag SHFgd4. Primary
259 SCs were infected 1 day after plating and fixed 3 days post-infection. Infected cells were
260 identified by GFP expression. Expression levels of FRABIN were evaluated by
261 immunofluorescence (in red). In contrast to non-infected cells (GFP negative, blue asterisks)

262 which express FRABIN, infected cells (GFP positive cells, yellow asterisks) are negative for
263 FRABIN.

264

265 **Supplementary Figure 4. Schematic figure summarizing the biochemical findings and**
266 **the proposed pathomechanisms underlying CMT4H pathology.** (A) Description of the
267 role of FRABIN in the regulation of the NRG1-type III-ERBB2/3 pathway and endocytic
268 trafficking in control conditions. The NRG1-type III-ERBB2/3/AKT/mTOR pathway is one
269 of the main pathways regulating myelination thickness through the expression of myelin and
270 lipid genes. ERBB2/3 levels are mainly regulated through endocytic trafficking. Through its
271 two phosphoinositides binding domains, FRABIN interacts and/or regulates key factors
272 involved in endosomal trafficking such as SNX3, RAB11 and, RAB11FIP2, promoting either
273 ERBB2/3 degradation through lysosomes or its recycling back to the membrane through
274 recycling endosomes. (B) Loss of FRABIN impairs NRG1-type III-ERBB2/3/AKT/mTOR
275 and endocytic trafficking, leading to hypermyelination (i.e generation of outfoldings). Loss of
276 FRABIN leads to an increase of key proteins regulating endosomal trafficking (SNX3,
277 RAB11 and, RAB11FIP2), consequently accelerating endosomal recycling and the presence
278 of ERBB2/3 receptors at the membrane surface. The increase of ERBB2/3 receptors leads to
279 an increase in AKT/mTOR pathway and may finally promote the expression of genes
280 controlling lipid production, a key constituent of the myelin sheet, as well as others genes such
281 as RAB11FIP2, a regulator of endosomal trafficking, as well as ERBIN, an adaptor protein
282 for ERBB2 receptor, ensuring its proper localization on the membrane.

283 **Supplementary Figure 5. Full western-blot membranes related to Figures 2 and 4.**

284 (A-D) Western blot pictures illustrating the expression of P-ERBB2, P-AKT, AKT, and the
285 related protein control GAPDH in *Fgd4^{SC-/-}* and control cocultures conditions (see **Figure 2**).
286 The yellow rectangle represents the western blot part used in each corresponding Figure. (E-
287 G) Western blot pictures illustrating the expression of ERBB2, mTOR and the related protein
288 control GAPDH in *Fgd4^{SC-/-}* and control cocultures conditions (see **Figure 2**). The yellow
289 rectangle represents the western blot part used in each corresponding Figure. (H-J) Western
290 blot pictures illustrating the expression of mTOR, ERBB2, and the related protein control
291 GAPDH, in the sciatic nerves of *Fgd4^{SC-/-}* and control animals (see **Figure 2**). The yellow
292 rectangle represents the western blot part used in each corresponding Figure. (K-M) Western
293 blot pictures illustrating the expression of P-AKT, AKT, and the related protein control

294 GAPDH, in the sciatic nerves of *Fgd4^{SC-/-}* and control animals (see **Figure 2**). The yellow
295 rectangle represents the western blot part used in each corresponding Figure (**N-O**) Western
296 blot pictures illustrating the expression of RAB11 as well as the related protein control
297 GAPDH in *Fgd4^{SC-/-}* and control cocultures conditions (see **Figure 4**). The yellow rectangle
298 represents the western blot part used in each corresponding Figure. (**P-Q**) Western blot
299 pictures illustrating the expression of RAB5 as well as the related protein control GAPDH in
300 *Fgd4^{SC-/-}* and control cocultures conditions (see **Figure 4**). The yellow rectangle represents
301 the western blot part used in each corresponding Figure.

302

303

304 **Supplementary Figure 6. Full western-blot membranes related to Figures 5, 6 and**

305 **Supplementary Figures 1 and 2.**

306 (**A**) Western blot picture illustrating the immunoprecipitation of SNX3 and FRABIN in
307 HEK293 cells overexpressing V5-tagged FRABIN. SNX3 was detected using an anti-SNX3
308 antibody after immunoprecipitation of V5-FRABIN using an anti-V5 antibody (see **Figure 5**).
309 The yellow rectangle represents the western blot part used in the corresponding Figure. (**B-C**)
310 Western blot pictures illustrating the expression of SNX3 and the related protein control
311 Tubulin in *Fgd4^{SC-/-}* and control cocultures conditions (see **Figure 4**). (**D-E**) Full western blot
312 pictures illustrating the expression of ERBIN, MAF1 (see **Supplementary Figure 2**), SNX3
313 (see **Figure 5**), and the related protein control GAPDH, in the sciatic nerves of *Fgd4^{SC-/-}* and
314 control animals. The yellow rectangle represents the western blot part used in each
315 corresponding Figure. (**F-H**) Western blot pictures illustrating the expression of P-ERBB2,
316 ERBB2 and the related protein control GAPDH in *Fgd4^{SC-/-}* and control cocultures conditions
317 (see **Figure 6**). The yellow rectangle represents the western blot part used in each
318 corresponding Figure. (**I-J**) Western blot pictures illustrating the expression of cleaved and
319 full-length Neuregulin 1-type III and the related protein control Tubulin in *Fgd4^{SC-/-}* and
320 control cocultures conditions (see **Supplementary Figure 1**). The yellow rectangle represents
321 the western blot part used in each corresponding Figure. (**K-L**) Full western blot pictures
322 illustrating the expression of cleaved and full-length Neuregulin 1-type III and the related
323 protein control GAPDH in the sciatic nerves of *Fgd4^{SC-/-}* and control animals (see
324 **Supplementary Figure 1**). (**M**) Western blot pictures illustrating the expression of SNX3 in
325 primary rat SCs infected with Lentivirus-SHcontrol, LV-SH-SNX3-1 or 2 (see
326 **Supplementary Figure 3**). The yellow rectangle represents the western blot part used in each
327 corresponding Figure.

328

329 **Supplementary Table1. Results of Differential Gene Expression analysis for a selected**
330 **list of genes involved in pathways relevant to PNS myelination.**

331 Genes with significant deregulation are highlighted in bold (padj value<0.05). A Fold Change
332 (FC) threshold of 1.5 and 0.5 has been chosen for up- and down-regulation respectively.

333 **Genes with padj<0.05 and FC >1.5 or <0.5 are in highlighted in bold blue.**

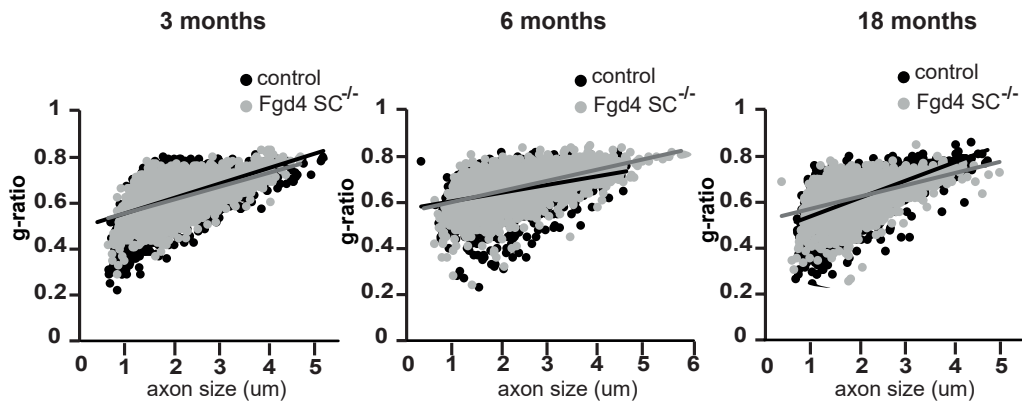
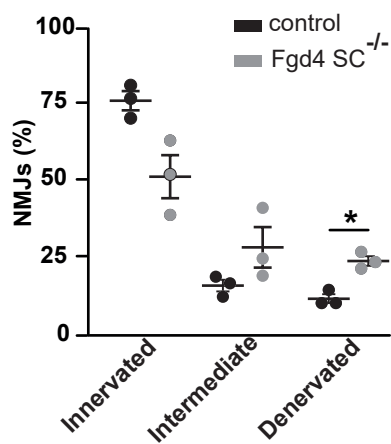
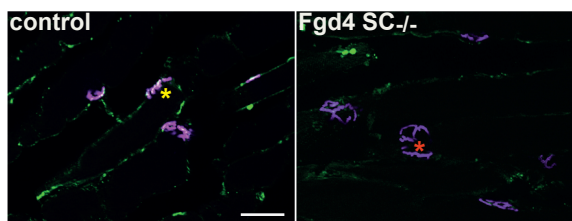
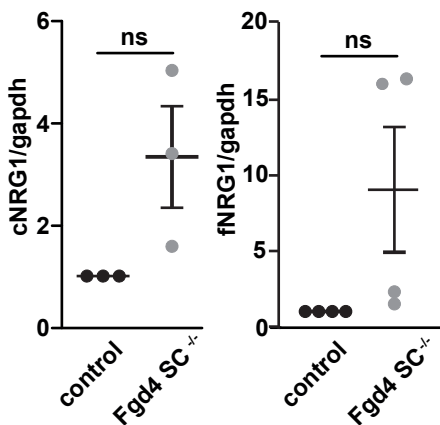
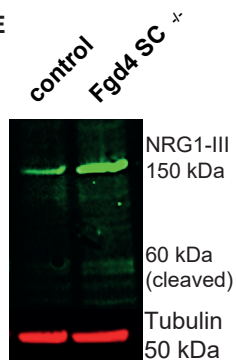
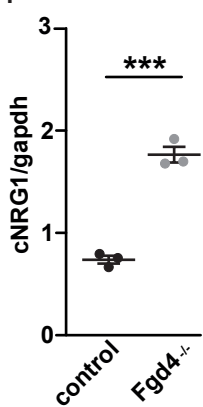
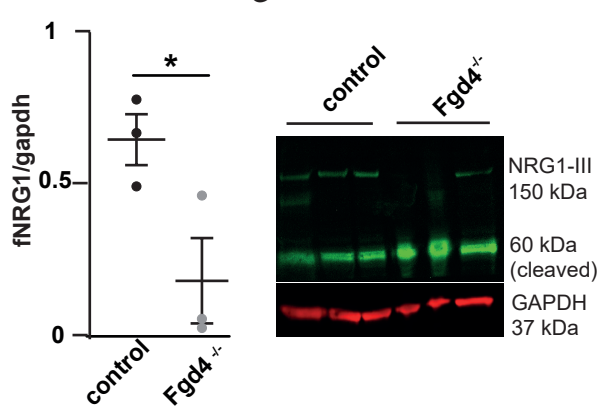
334 *FC=Fold Change; padj=adjusted value. Basemean represents the average of the normalized*
335 *count values, dividing by size factors, taken over all samples. Pvalue=P-value of the test for*
336 *the gene or transcript. padj=Adjusted P-value for multiple testing for the gene or*
337 *transcript.NA=Not Assessed*

338

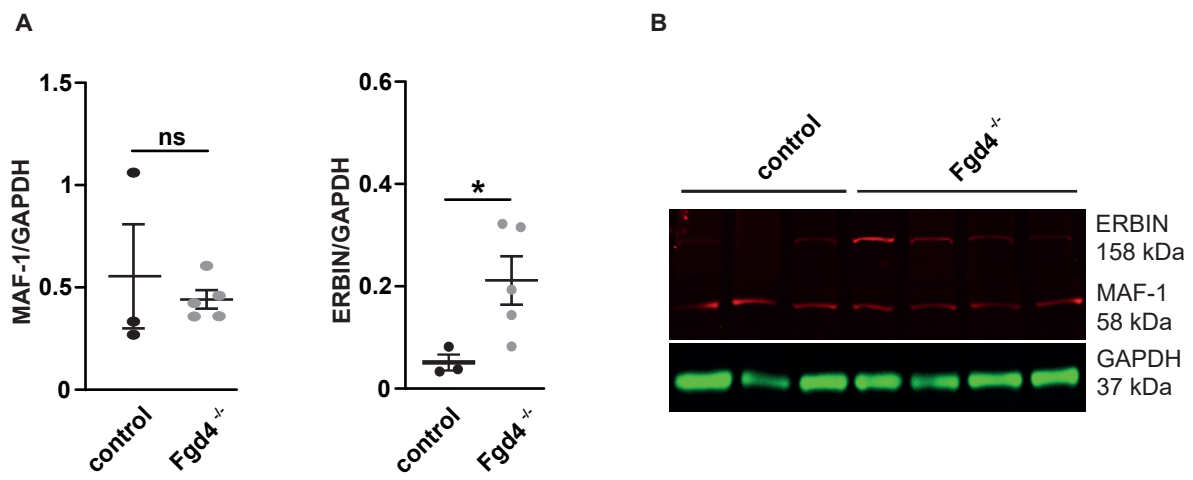
339 **References**

- 340 1. Bernard-Marissal N, van Hameren G, Juneja M, et al. Altered interplay between
341 endoplasmic reticulum and mitochondria in Charcot-Marie-Tooth type 2A neuropathy.
342 Research Support, Non-U.S. Gov't. *Proc Natl Acad Sci U S A*. Feb 5 2019;116(6):2328-2337.
343 doi:10.1073/pnas.1810932116
- 344 2. Arnaud E, Zenker J, de Preux Charles AS, et al. SH3TC2/KIAA1985 protein is
345 required for proper myelination and the integrity of the node of Ranvier in the peripheral
346 nervous system. *Proc Natl Acad Sci U S A*. Oct 13 2009;106(41):17528-33.
347 doi:10.1073/pnas.0905523106
- 348 3. Horn M, Baumann R, Pereira JA, et al. Myelin is dependent on the Charcot-Marie-
349 Tooth Type 4H disease culprit protein FRABIN/FGD4 in Schwann cells. Research Support,
350 Non-U.S. Gov't. *Brain*. Dec 2012;135(Pt 12):3567-83. doi:10.1093/brain/aws275
- 351 4. Walhout AJ, Vidal M. High-throughput yeast two-hybrid assays for large-scale protein
352 interaction mapping. *Methods*. Jul 2001;24(3):297-306. doi:10.1006/meth.2001.1190

353

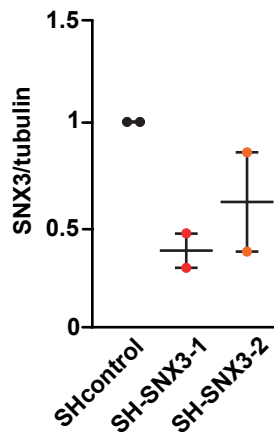
A**B****C****D****E****F****G**

Supplementary Figure 1

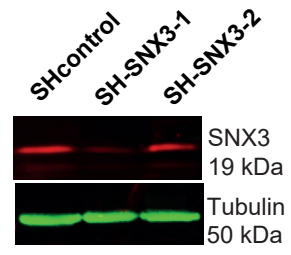


Supplementary Figure 2

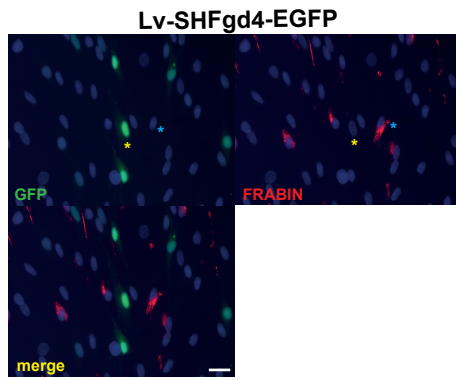
A



B

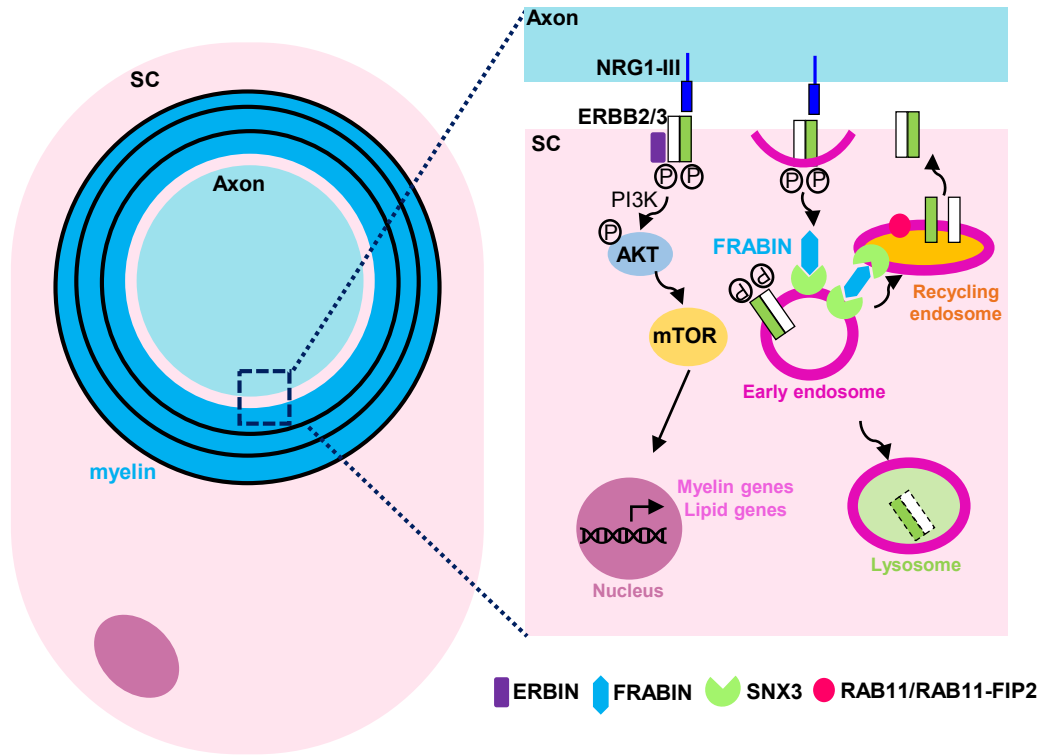


C

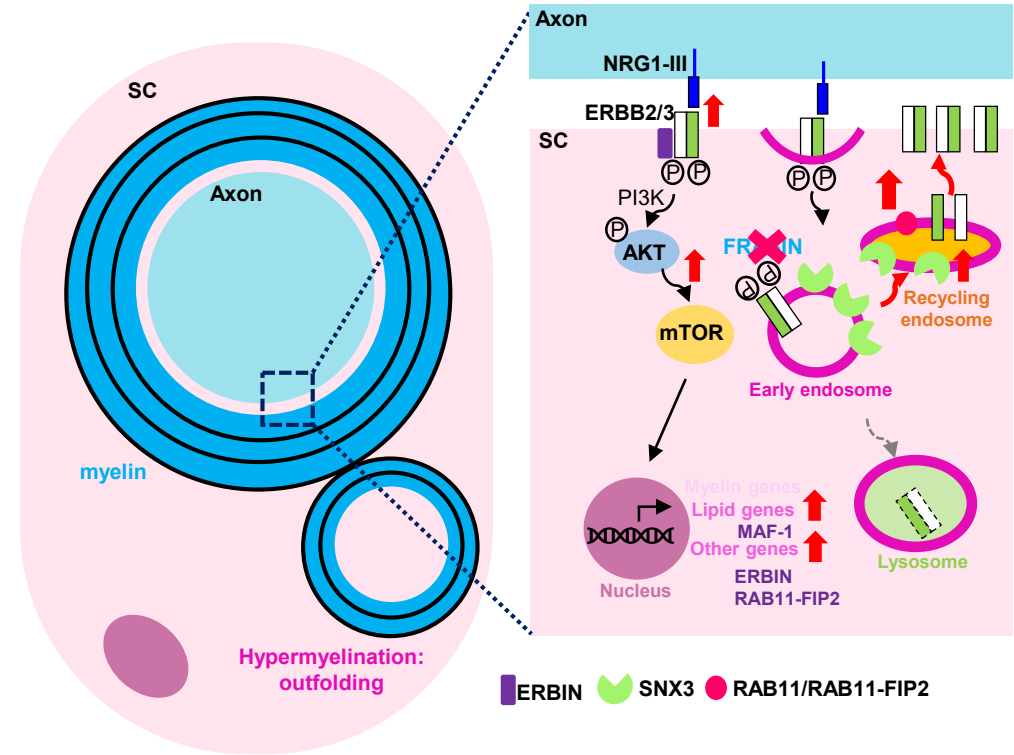


Supplementary Figure 3

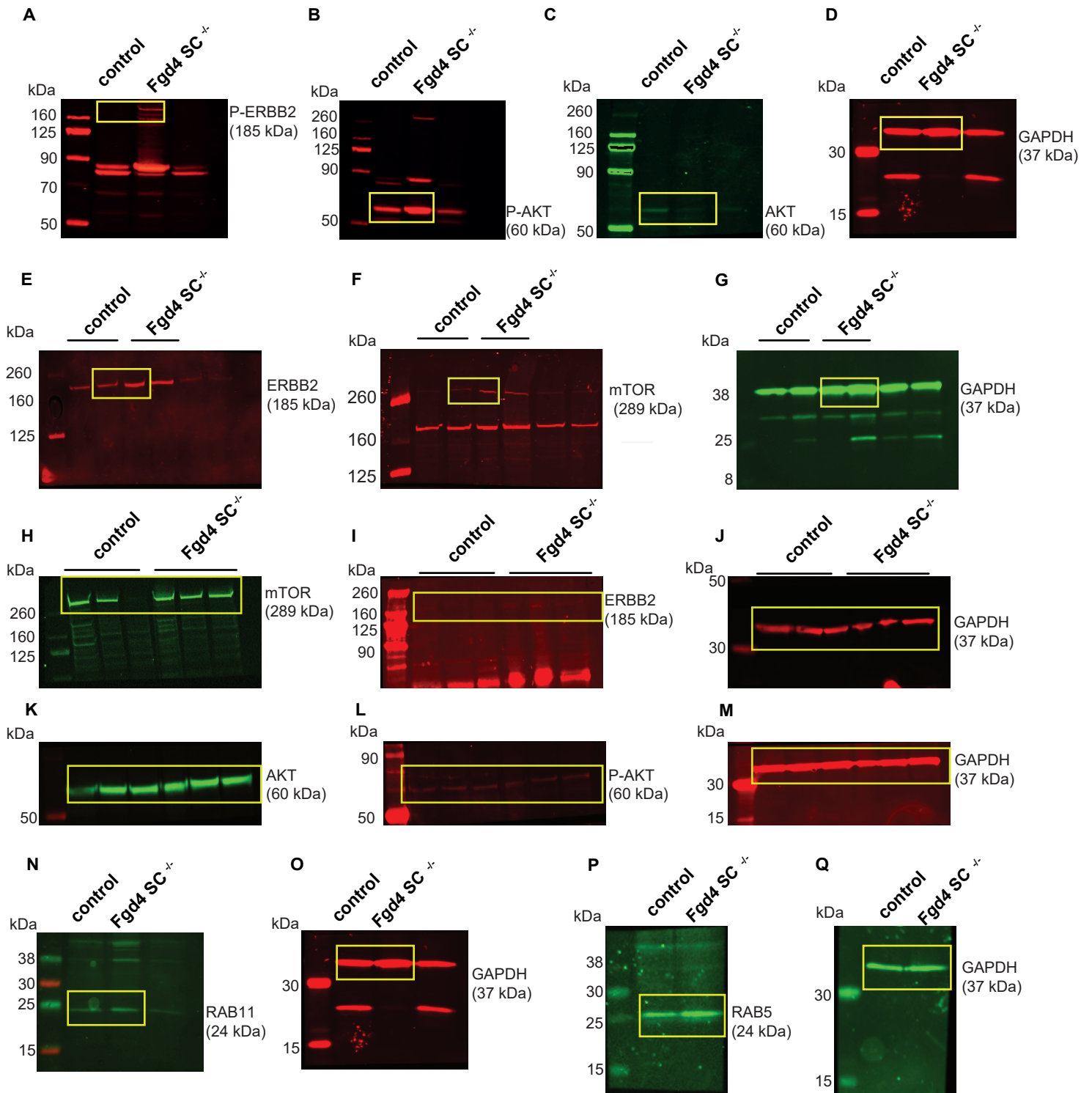
A. control



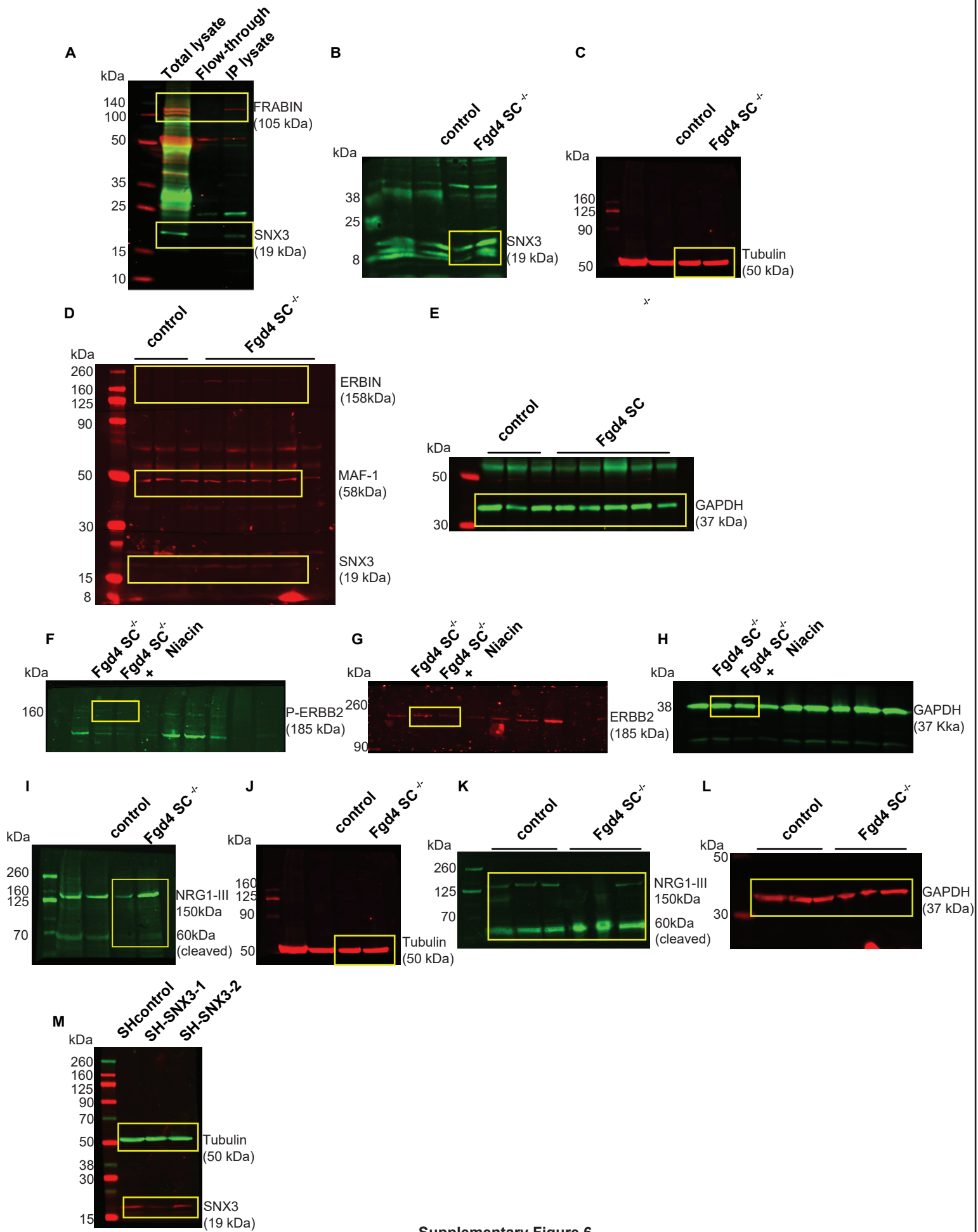
B. *Fgd4*^{SC-/-}



Supplementary Figure 4



Supplementary Figure 5



Supplementary Figure 6

padj	pvalue	Ensembl ID	HGNC Gene symbol	baseMean	log2(FC)	FC
NRG1-EBB2-3 pathway						
0.43819	0.180994	ENSMUSG00000062991.7 Nrg1	<i>Nrg1</i>	118.948	-0.54732	0.68429
0.28716	0.088773	ENSMUSG00000032311.17 Nrg4	<i>Nrg4</i>	26.50165	-1.31886	0.400852
0.141851	0.030578	ENSMUSG00000062312.5 ErbB2	<i>ErbB2</i>	3855.963	0.366331	1.28907
0.006345	0.000445	ENSMUSG00000018166.8 ErbB3	<i>ErbB3</i>	7345.251	0.487969	1.402469
0.472484	0.206585	ENSMUSG00000062209.15 ErbB4	<i>ErbB4</i>	40.39399	-0.86434	0.549299
0.000342	1.18E-05	ENSMUSG00000021709.14 Erbin	<i>Erbin</i>	10892.24	0.72783	1.656146
0.086574	0.015001	ENSMUSG00000013663.7 Pten	<i>Pten</i>	12586.44	0.300629	1.231681
0.041169	0.005329	ENSMUSG00000022770.16 Dlg1	<i>Dlg1</i>	7211.615	0.456034	1.371765
0.124126	0.025167	ENSMUSG00000041417.15 Pik3r1	<i>Pik3r1</i>	12356	0.292736	1.224961
0.162919	0.037558	ENSMUSG00000034614.14 Pik3ip1	<i>Pik3ip1</i>	2432.501	-0.32628	0.797592
0.374588	0.138018	ENSMUSG00000028698.13 Pik3r3	<i>Pik3r3</i>	2474.129	0.228918	1.171955
0.435797	0.179052	ENSMUSG00000033628.15 Pik3c3	<i>Pik3c3</i>	1632.136	0.217502	1.162719
0.485684	0.216219	ENSMUSG00000032571.14 Pik3r4	<i>Pik3r4</i>	2075.567	0.17431	1.128425
0.711939	0.44546	ENSMUSG00000031834.15 Pik3r2	<i>Pik3r2</i>	3950.073	0.105829	1.076112
0.721107	0.456363	ENSMUSG00000032462.14 Pik3cb	<i>Pik3cb</i>	433.0512	0.217911	1.163048
0.996264	0.989948	ENSMUSG00000026447.16 Pik3c2b	<i>Pik3c2b</i>	276.4396	-0.00377	0.99739
NA	0.015473	ENSMUSG00000046207.14 Pik3r6	<i>Pik3r6</i>	5.920665	5.729172	53.04601
6.29E-06	9.37E-08	ENSMUSG00000030660.9 Pik3c2a	<i>Pik3c2a</i>	3826.552	0.977572	1.969149
1.34E-05	2.35E-07	ENSMUSG00000025017.9 Pik3ap1	<i>Pik3ap1</i>	461.9112	2.25651	4.778342
7.35E-05	1.79E-06	ENSMUSG00000020573.17 Pik3cg	<i>Pik3cg</i>	117.1629	3.574393	11.91241
0.009386	0.000736	ENSMUSG00000039936.18 Pik3cd	<i>Pik3cd</i>	674.6376	0.635754	1.553749
0.020476	0.002102	ENSMUSG00000020901.13 Pik3r5	<i>Pik3r5</i>	378.2187	1.176062	2.259592
0.03711	0.004613	ENSMUSG00000027665.13 Pik3ca	<i>Pik3ca</i>	5124.153	0.377022	1.298659
0.891783	0.741992	ENSMUSG00000001729.14 Akt1	<i>Akt1</i>	9988.497	0.039302	1.027616
0.96188	0.905924	ENSMUSG0000004056.15 Akt2	<i>Akt2</i>	7633.627	0.016005	1.011156
0.039456	0.005015	ENSMUSG00000019699.16 Akt3	<i>Akt3</i>	3501.403	0.387865	1.308455
0.580322	0.297197	ENSMUSG00000028161.17 Ppp3ca	<i>Ppp3ca</i>	8459.122	0.12355	1.089412

0.791934	0.558113	ENSMUSG00000022092.10 Ppp3cc	<i>Ppp3cc</i>	681.3545	-0.11055	0.926235
0.876171	0.708198	ENSMUSG00000028310.2 Ppp3r2	<i>Ppp3r2</i>	13.4879	-0.40122	0.757217
0.070239	0.011147	ENSMUSG00000021816.11 Ppp3cb	<i>Ppp3cb</i>	4763.976	0.345142	1.270276
0.654851	0.372752	ENSMUSG00000059923.13 Grb2	<i>Grb2</i>	3646.282	0.114613	1.082685
0.749643	0.497543	ENSMUSG00000016933.17 Plcg1	<i>Plcg1</i>	4356.898	0.090765	1.064935
0.015597	0.001445	ENSMUSG00000034330.10 Plcg2	<i>Plcg2</i>	146.1442	1.944124	3.848041
0.30888	0.100147	ENSMUSG00000042626.13 Shc1	<i>Shc1</i>	9074.716	0.216848	1.162192
0.745429	0.492031	ENSMUSG00000020312.12 Shc2	<i>Shc2</i>	1858.432	0.103934	1.0747
0.553667	0.272862	ENSMUSG00000035109.14 Shc4	<i>Shc4</i>	977.9834	0.233873	1.175988
0.808209	0.583182	ENSMUSG00000021448.7 Shc3	<i>Shc3</i>	69.73623	0.336288	1.262504
0.899781	0.757653	ENSMUSG00000022322.8 Shcbp1	<i>Shcbp1</i>	367.8136	-0.09946	0.933385
0.020802	0.00215	ENSMUSG00000031714.9 Gabl	<i>Gabl</i>	10659.16	0.390408	1.310764
0.894073	0.746486	ENSMUSG0000001847.14 Rac1	<i>Rac1</i>	16699.4	0.043314	1.030478
0.850086	0.658274	ENSMUSG00000006699.17 Cdc42	<i>Cdc42</i>	21798.67	-0.05597	0.961945
0.000462	1.73E-05	ENSMUSG00000024241.6 Sos1	<i>Sos1</i>	2598.422	0.628269	1.545709
0.955817	0.89115	ENSMUSG00000025225.14 Nfkb2	<i>Nfkb2</i>	1618.804	0.023708	1.016569
0.970434	0.924565	ENSMUSG00000030595.15 Nfkbib	<i>Nfkbib</i>	416.7245	0.022398	1.015646
0.340651	0.118227	ENSMUSG00000023947.7 Nfkbie	<i>Nfkbie</i>	489.3592	-0.3758	0.770676
0.343576	0.119708	ENSMUSG00000028163.17 Nfkb1	<i>Nfkb1</i>	3895.871	0.206704	1.154049
0.351699	0.12434	ENSMUSG00000035356.16 Nfkbiz	<i>Nfkbiz</i>	722.8807	0.386129	1.306882
0.624303	0.33987	ENSMUSG00000042419.8 Nfkbil1	<i>Nfkbil1</i>	329.5072	-0.25265	0.839354
0.631793	0.346968	ENSMUSG00000021025.8 Nfkbia	<i>Nfkbia</i>	1390.241	0.16228	1.119054
0.830571	0.621747	ENSMUSG00000036931.15 Nfkbid	<i>Nfkbid</i>	21.94257	0.447472	1.363649
0.916137	0.79385	ENSMUSG00000063065.13 Mapk3	<i>Mapk3</i>	7246.235	0.041078	1.028883
0.372786	0.137078	ENSMUSG00000063358.15 Mapk1	<i>Mapk1</i>	7794.191	0.188154	1.139305
0.019785	0.001995	ENSMUSG00000021754.17 Map3k1	<i>Map3k1</i>	1746.545	0.56038	1.474657
0.546057	0.266104	ENSMUSG00000035027.18 Map2k2	<i>Map2k2</i>	2303.944	-0.20246	0.869068
0.566792	0.284138	ENSMUSG00000052837.6 Junb	<i>Junb</i>	1418.494	-0.18866	0.877423
0.835999	0.632831	ENSMUSG00000071076.6 Jund	<i>Jund</i>	4019.524	-0.09702	0.934961

0.96498	0.910985	ENSMUSG00000052684.4 Jun	<i>Jun</i>	9504.418	0.013414	1.009341
0.243296	0.068482	ENSMUSG00000020516.15 Rps6kb1	<i>Rps6kb1</i>	2809.235	0.277378	1.21199
0.279578	0.085021	ENSMUSG00000028991.15 Mtor	<i>Mtor</i>	2649.592	0.235803	1.177562
0.247636	0.070246	ENSMUSG00000026812.16 Tsc1	<i>Tsc1</i>	1431.294	0.297643	1.229135
0.611303	0.327886	ENSMUSG00000002496.9 Tsc2	<i>Tsc2</i>	3582.222	0.127857	1.092669
0.00173	8.68E-05	ENSMUSG00000042406.7 Atf4	<i>Atf4</i>	7319.911	-0.57001	0.673613
0.001872	9.61E-05	ENSMUSG00000005667.8 Mthfd2	<i>Mthfd2</i>	1109.636	-0.90232	0.535026
0.011004	0.000912	ENSMUSG00000031490.6 Eif4ebp1	<i>Eif4ebp1</i>	1254.967	-0.66088	0.632493
0.762307	0.515451	ENSMUSG00000028156.12 Eif4e	<i>Eif4e</i>	3268.458	0.08441	1.060254
8.91E-05	2.27E-06	ENSMUSG00000003847.16 Nfat5	<i>Nfat5</i>	6856.594	0.709679	1.63544
0.023569	0.002554	ENSMUSG00000031902.10 Nfatc3	<i>Nfatc3</i>	4338.228	0.461474	1.376948
0.253156	0.072699	ENSMUSG00000023411.11 Nfatc4	<i>Nfatc4</i>	1795.49	-0.29686	0.814023
Endocytic trafficking						
0.293808	0.092099	ENSMUSG00000019804.12 Snx3	<i>Snx3</i>	4878.23	-0.24198	0.845583
0.002403	0.00013	ENSMUSG00000071669.14 Snx29	<i>Snx29</i>	406.6079	0.919201	1.891068
0.128409	0.026519	ENSMUSG00000022500.14 Litaf	<i>Litaf</i>	4149.401	-0.37776	0.769633
0.296879	0.093789	ENSMUSG00000017831.7 Rab5a	<i>Rab5a</i>	5292.429	0.225821	1.169442
0.57979	0.296661	ENSMUSG00000027637.3 110008F13Rik	<i>Rab5if</i>	1993.569	-0.17004	0.88882
0.642659	0.359081	ENSMUSG00000000711.3 Rab5b	<i>Rab5b</i>	6268.775	0.119281	1.086193
0.998431	0.995078	ENSMUSG00000019173.11 Rab5c	<i>Rab5c</i>	5851.344	-0.00077	0.999463
0.000378	1.35E-05	ENSMUSG00000040022.14 Rab11fip2	<i>Rab11fip2</i>	1744.883	0.764147	1.698365
0.41397	0.163463	ENSMUSG00000017639.13 Rab11fip4	<i>Rab11fip4</i>	277.7209	-0.57684	0.67043
0.886834	0.730381	ENSMUSG00000037098.17 Rab11fip3	<i>Rab11fip3</i>	2391.225	0.048893	1.034471
0.901869	0.763519	ENSMUSG00000031488.14 Rab11fip1	<i>Rab11fip1</i>	99.6553	0.146736	1.107062
0.997491	0.992665	ENSMUSG00000004771.12 Rab11a	<i>Rab11a</i>	3994.743	-0.00141	0.999025
0.908187	0.780765	ENSMUSG00000077450.12 Rab11b	<i>Rab11b</i>	5658.079	-0.03805	0.973969
0.941931	0.851932	ENSMUSG00000051343.11 Rab11fip5	<i>Rab11fip5</i>	2767.754	-0.02548	0.982492
Myelin genes						
0.898169	0.754411	ENSMUSG00000056569.10 Mpz	<i>Mpz</i>	21482.08	-0.22693	0.854452

0.144957	0.031642	ENSMUSG00000018217.12 Pmp22	<i>Pmp22</i>	16422.81	-0.49145	0.71131
0.680595	0.403483	ENSMUSG00000041607.16 Mbp	<i>Mbp</i>	10741.13	-0.6543	0.635384
0.552567	0.271691	ENSMUSG00000036634.15 Mag	<i>Mag</i>	382.9271	-1.24442	0.422078
0.377353	0.139799	ENSMUSG00000047797.14 Gjb1	<i>Gjb1</i>	13.37527	1.909331	3.756348
0.762179	0.515278	ENSMUSG00000037868.15 Egr2	<i>Egr2</i>	1131.125	0.163869	1.120288
0.622139	0.337443	ENSMUSG00000033006.9 Sox10	<i>Sox10</i>	7814.012	0.17023	1.125238
0.407887	0.159458	ENSMUSG00000090125.3 Pou3f1	<i>Pou3f1</i>	336.5669	0.577193	1.491943
0.210427	0.054811	ENSMUSG00000095139.2 Pou3f2	<i>Pou3f2</i>	137.4265	-0.92968	0.524976
0.704889	0.436666	ENSMUSG00000052468.7 Pmp2	<i>Pmp2</i>	838.2964	-0.32763	0.796846
0.530544	0.253464	ENSMUSG00000053198.13 Prx	<i>Prx</i>	2837.423	-0.36805	0.774827
Lipid metabolism and cholesterol synthesis						
8.21E-05	2.06E-06	ENSMUSG00000055435.6 Maf	<i>Maf</i>	6049.204	0.657916	1.577801
0.545362	0.265642	ENSMUSG00000020538.15 Srebfl	<i>Srebfl</i>	4318.675	0.190077	1.140825
0.765008	0.519542	ENSMUSG00000022463.7 Srebfl2	<i>Srebfl2</i>	8066.606	0.082783	1.059059
ECM/integrins						
3.88E-05	8.31E-07	ENSMUSG00000027111.15 Itga6	<i>Itga6</i>	12394.81	0.982093	1.97533
2.90E-09	1.70E-11	ENSMUSG00000039115.13 Itga9	<i>Itga9</i>	7156.76	0.905284	1.872913
0.000474	1.79E-05	ENSMUSG00000030786.18 Itgam	<i>Itgam</i>	507.6395	4.037302	16.41909
0.000492	1.88E-05	ENSMUSG00000032243.8 Itga11	<i>Itga11</i>	1407.479	-0.81339	0.569043
0.001767	8.95E-05	ENSMUSG00000030830.18 Itgal	<i>Itgal</i>	100.9593	3.273645	9.670868
0.003732	0.000229	ENSMUSG00000027087.11 Itgav	<i>Itgav</i>	9771.51	0.43798	1.354706
0.012968	0.001124	ENSMUSG00000090210.7 Itga10	<i>Itga10</i>	640.1986	-0.73403	0.601221
0.066913	0.010474	ENSMUSG00000027009.18 Itga4	<i>Itga4</i>	381.0249	0.63189	1.549593
0.127424	0.026148	ENSMUSG00000026768.10 Itga8	<i>Itga8</i>	5094.602	0.53972	1.453691
0.299509	0.095298	ENSMUSG0000000555.7 Itga5	<i>Itga5</i>	4157.454	-0.2217	0.857554
0.354608	0.126038	ENSMUSG00000034664.13 Itga2b	<i>Itga2b</i>	173.4799	-0.57587	0.67088
0.598459	0.315172	ENSMUSG0000001507.16 Itga3	<i>Itga3</i>	1174.635	0.180398	1.133197
0.641351	0.357489	ENSMUSG00000042284.10 Itga1	<i>Itga1</i>	14742	0.142267	1.103638
0.943815	0.857184	ENSMUSG00000015533.9 Itga2	<i>Itga2</i>	1249.488	0.03837	1.026953

0.996754	0.991393	ENSMUSG00000025348.9 Itga7	<i>Itga7</i>	8358.219	-0.0015	0.99896
9.88E-20	1.07E-22	ENSMUSG00000025321.14 Itgb8	<i>Itgb8</i>	19569.38	1.176076	2.259613
7.32E-07	8.29E-09	ENSMUSG0000000290.13 Itgb2	<i>Itgb2</i>	228.669	3.307438	9.900066
0.0031	0.000179	ENSMUSG00000020689.4 Itgb3	<i>Itgb3</i>	2213.103	0.581636	1.496545
0.056372	0.008227	ENSMUSG00000022817.14 Itgb5	<i>Itgb5</i>	6858.318	-0.51889	0.697907
0.447299	0.186731	ENSMUSG00000025809.15 Itgb1	<i>Itgb1</i>	64736.22	0.157445	1.11531
0.491626	0.220459	ENSMUSG00000028549.17 Itgb3bp	<i>Itgb3bp</i>	298.5605	-0.35543	0.781634
0.653405	0.371103	ENSMUSG00000020758.15 Itgb4	<i>Itgb4</i>	9286.396	0.160876	1.117965
0.785845	0.549528	ENSMUSG00000062352.13 Itgb1bp1	<i>Itgb1bp1</i>	1146.963	-0.09858	0.93395
0.853009	0.664619	ENSMUSG0000001281.9 Itgb7	<i>Itgb7</i>	300.1425	0.1541	1.112727
0.856983	0.671372	ENSMUSG00000032925.16 Itgb11	<i>Itgb11</i>	9900.586	-0.07517	0.949233
0.747194	0.494004	ENSMUSG00000019899.16 Lama2	<i>Lama2</i>	12565.15	-0.09002	0.939512
0.937544	0.843337	ENSMUSG0000002900.16 Lamb1	<i>Lamb1</i>	19794.36	-0.03484	0.97614
0.400955	0.155105	ENSMUSG00000026478.14 Lamc1	<i>Lamc1</i>	32910.12	0.177825	1.131177
0.918246	0.797716	ENSMUSG00000022607.14 Ptk2	<i>Ptk2</i>	4506.624	0.031356	1.021972
GPCR signaling						
9.82E-05	2.54E-06	ENSMUSG00000063234.4 Gpr84	<i>Gpr84</i>	28.17772	7.978702	252.2485
0.000138	3.93E-06	ENSMUSG00000040133.2 Gpr176	<i>Gpr176</i>	695.3308	-1.13642	0.454888
0.010094	0.000815	ENSMUSG00000021886.7 Gpr65	<i>Gpr65</i>	42.05601	3.398591	10.54576
0.022427	0.002378	ENSMUSG00000040836.15 Gpr161	<i>Gpr161</i>	1346.138	0.52714	1.441069
0.041099	0.005306	ENSMUSG00000046961.7 Gpr156	<i>Gpr156</i>	131.4803	-1.51648	0.349539
cAMP signaling						
2.56E-08	1.85E-10	ENSMUSG00000022376.7 Adcy8	<i>Adcy8</i>	131.2815	-2.55334	0.17036
1.95E-05	3.72E-07	ENSMUSG00000005580.11 Adcy9	<i>Adcy9</i>	531.147	1.20252	2.301413
0.00027	8.96E-06	ENSMUSG00000031659.13 Adcy7	<i>Adcy7</i>	8184.577	0.688989	1.612153
0.007014	0.000502	ENSMUSG00000024256.6 Adcyap1	<i>Adcyap1</i>	418.6966	1.101277	2.145444
0.009386	0.000735	ENSMUSG00000022840.8 Adcy5	<i>Adcy5</i>	2227.753	0.540373	1.454348
9.38E-09	5.92E-11	ENSMUSG00000029778.12 Adcyap1r1	<i>Adcyap1r1</i>	1375.504	1.240339	2.36254
Other signaling pathways						

0.003026	0.000172	ENSMUSG00000015340.10 Cybb	Cybb	413.9266	4.116552	17.34625
0.011383	0.000949	ENSMUSG00000042286.13 Stab1	Stab1	1920.658	2.782242	6.879205
0.005292	0.00035	ENSMUSG00000024401.14 Tnf	Tnf	26.17281	4.397772	21.07954
0.005004	0.000328	ENSMUSG00000045382.6 Cxcr4	Cxcr4	141.6688	-1.44541	0.367187

Supplementary Table1. Results of Differential Gene Expression analysis for a selected list of genes involved in pathways relevant to PNS myelination.

Genes with significant deregulation are highlighted in bold (padj value<0.05). A Fold Change (FC) threshold of 1.5 and 0.5 has been chosen for up- and down-regulation respectively. **Genes with padj<0.05 and FC >1.5 or <0.5 are in highlighted in bold blue.**

FC=Fold Change; padj=adjusted value. Basemean represents the average of the normalized count values, dividing by size factors, taken over all samples. Pvalue=P-value of the test for the gene or transcript. padj=Adjusted P-value for multiple testing for the gene or transcript.NA=Not Assessed